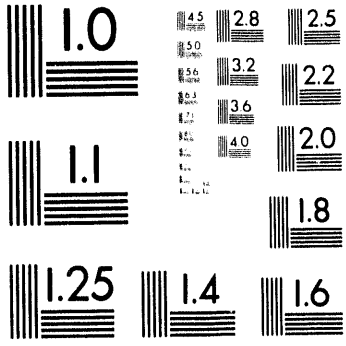
1.0
1.1
1.25
1.4
1.6
1.8
2.0
2.2
2.5
2.8
3.2
3.6
4.0
4.5
5.0
5.6

1 of 1

SAND93-0610
Unlimited Release
Printed September 1993

Distribution
Category UC-704

Dynamic Properties of Ceramic Materials

D. E. Grady
Experimental Impact Physics Department 1433

J. L. Wise
Geothermal Research Department 6111

Sandia National Laboratories
Albuquerque, NM 87185

Abstract

Controlled impact methods have been employed to obtain dynamic response properties of armor materials. The purpose of this work has been to provide material-property support for computational and analytical assessments of ceramic performance in engineering applications. In particular, new experimental data have been obtained for high-strength ceramics. Continued analysis of time-resolved velocity interferometer measurements has produced systematic material-property data for Hugoniot and release response, initial and post-yield strength, pressure-induced phase transformation, and dynamic fracture strength. A new technique has been developed to measure hydrodynamic properties of ceramic through shock-wave experiments on metal-ceramic composites, and unique data have been obtained for silicon carbide. Additional data on several titanium diboride ceramics and high-quality aluminum oxide ceramic have been acquired, and issues regarding the influence of microstructure on dynamic properties have emerged. A systematic comparison of dynamic (Hugoniot elastic limit) strength and indentation hardness data has been performed, and important correlations have been revealed. Innovative impact experiments on confined and unconfined alumina rods using axial and transverse VISAR diagnostics have been demonstrated which permit the acquisition of multiaxial dynamic response data. The dynamic failure properties of a high-density aluminosilicate glass, similar in composition to the intergranular glassy phase of some aluminas, have been investigated with regard to yield, spall, and failure-wave propagation.

Sponsored by the U.S. Department of Energy and conducted under the auspices of the U. S. Department of Energy under Contract DE-AC04-76DP00789.

Acknowledgments

A large portion of the present research has received significant stimulus and guidance from other laboratories and workers. It is appropriate to acknowledge these interactions which have been responsible in large measure for a number of the positive aspects of the study.

The additional shock compression data on titanium diboride is a consequence of a visit of one of us (DEG) with Wolf-Dieter Winkler of the Ernst Mach Institut in the fall of 1991. Discussions concerning mechanisms of the double yield observed in this material resulted in the reported further testing of a sample of the EMI TiB_2. The insights of Wolf-Dieter Winkler on shock deformation properties of TiB_2 are gratefully acknowledged.

Extensive indentation hardness testing of the suite of ceramics investigated under shock loading at Sandia over the past several years was undertaken by Michael Slavin of the Army Research Laboratory. His detailed knowledge of static hardness mechanisms contributed significantly to the value of this study.

The shock wave strength measurements on the Michigan Technological University aluminum oxide were initiated by Jim Staehler and Bill Predebon of that Institution. The study contributed to the PhD research of Dr. Staehler and has added to our knowledge of the shock properties of this material.

Studies of dynamic fracture and failure waves resulted from a collaboration of one of us (JLW) with George Raiser and Rod Clifton of Brown University. We gratefully acknowledge their impetus and guidance in completing this fruitful study.

Contents

1. Introduction and Summary

The current program focuses on the measurement of response properties of high-strength ceramic materials to support modeling activities facilitating computational and engineering analyses of ceramic structures under dynamic loads. As material response models and calculational methods mature they play an increasingly important role as cost-effective and time-efficient tools for the design, optimization, and evaluation of such structures.

The necessary material response models are currently in a state of rapid development. Consequently, the present material properties testing program performs two crucial functions: First, the deformation mechanisms experienced by materials subjected to transient loads, which must be described in appropriate dynamic material response models, are being identified and characterized through high-resolution testing methods. Second, with the on-going development of response models for different material classes, the dynamic material testing provides quantitative material property data for model validation. A close interaction between calculational material-response modeling activities and dynamic material-property testing studies of the type discussed herein is essential to the successful attainment of the program objectives.

The baseline material property study in this program has used established, state-of-the-art, controlled impact methods along with high-resolution velocity interferometry diagnostics to provide the highest quality material property data under conditions of high-rate and high-confining-pressure loading. These data provide the backbone equation-of-state, strength, and dynamic fracture information needed to constrain dynamic response models for specific materials.

The program has also included technical development efforts to extend high-resolution, controlled impact methods to a broader range of dynamic loading conditions. Impact experiments on confined and unconfined ceramic rods using transverse and axial VISAR diagnostics have been developed to explore multiaxial material response properties. Shock studies on ceramic-metal composites have been pursued to determine the high-pressure hydrodynamic response of ceramics.

Specific program objectives have included continued investigation of the high-pressure equation-of-state, strength, and fracture properties of monolithic ceramics. A comparative study of dynamic strength with indentation hardness measurements has been performed, and a new experimental method was developed for measuring the hydrodynamic properties of ceramics. Significant progress has been achieved for measuring multiaxial properties of ceramics and the dynamic failure properties of high-density glass have been investigated.

Program goals which have been successfully achieved include the following:

Further equation-of-state testing on titanium diboride ceramic from several sources (in cooperation with Ernst-Mach Institute) and on high-quality aluminum oxide ceramic (in cooperation with Michigan Technological University) has led to increased

understanding of material property dependence on microstructure. Important influences of porosity and grain size on dynamic strength properties of these ceramics have been measured.

Indentation hardness measurements (in cooperation with the Army Materials Laboratory) have been performed on ceramics for which high-resolution VISAR shock-wave data have been obtained. This study has provided a detailed comparison of dynamic and static strength properties of armor ceramics. Although not yet definitive, important correlations are noted which may lead to an overlap of test techniques.

Significant progress has been made in the measurement of the hydrodynamic compression of ceramic through shock-wave experiments on metal-ceramic composites. A series of experiments has been completed on silicon carbide and copper mixtures, and analysis of this data has been performed. Data for shock pressures in excess of 20 GPa were consistent with hydrodynamic response and agreed with extrapolations of ultrasonic measurements. Shock measurements in the 10-15 GPa range exhibited unexpected metal-ceramic composite strength and may lead to further interest in composite material properties.

The development of techniques for determining dynamic multiaxial properties of ceramics has proceeded at an encouraging pace. A series of impact experiments on confined and unconfined ceramic rods using axial and transverse VISAR diagnostics has been completed. Extended (tens-of-microseconds) recording times have been achieved. The data are being analyzed to provide partial-confinement dynamic strength and fracture-wave properties.

Experiments have been performed on high-density glass (in cooperation with Brown University) to achieve improved understanding of dynamic failure mechanisms in ceramics. Tests were conducted to determine initiation and propagation characteristics of fracture-damage failure waves in glass. Spall properties of shock-damaged material were also explored.

2. Shock Compression Properties of Titanium Diboride Ceramics

During the course of the present program extensive shock compression and release properties have been obtained on titanium-diboride ceramic from two different suppliers. More recent shock data have been obtained on titanium-diboride ceramic supplied by the Army Materials Technology Laboratory and reduction of this data is in progress. In addition, samples of a titanium-diboride ceramic reported to have unusual strength properties were obtained from the Ernst-Mach Institute in Freiburg, Germany and also tested.

The principal difference in the ceramics tested involved the material microstructure, and the present dynamic property experiments have revealed important consequences. Significant strength differences due to variations and distributions in microstructural porosity were noted. Effects due to differences in microstructure grain size were also observed.

Materials

Shock-compression and strength results on two TiB_2 ceramics having markedly different microstructures have been reported by Winkler and Stilp (1992). The preponderance of experiments was performed on a relatively coarse grain ceramic (grain size 30-50 μm) in which porosity was mainly included in grains (intracrystalline porosity). A second material was also tested in which the grain size was significantly smaller (grain size = 5-10 μm) and porosity was primarily localized to triple-grain junctions (intercrystalline porosity). The initial density of both materials was 4360 ±30 kg/m^3 which implies a porosity of about 4-5% based strictly on density considerations. The coarse-grain and fine-grain samples from Ernst-Mach Institute will be referred to as EMI-1 and EMI-2, respectively.

Titanium-diboride ceramics from two suppliers have also been investigated for shock-compression properties at Sandia National Laboratories. The two materials had initial densities of 4452 kg/m^3 and 4509 kg/m^3 and will be referred to as SNL-1 and SNL-2, respectively. A grain size of about 10-25 μm for SNL-1 and a somewhat larger grain size of about 20-50 μm for SNL-2 was determined from optical metallography. Metallography also indicated that porosity resided mainly on grain boundaries (intercrystalline porosity) for both SNL materials and the porosity was somewhat lower for SNL-2, consistent with the density difference between the SNL materials. Both SNL materials were similar to material EMI-2 in terms of the microstructural nature of the porosity.

Experiments

All shock-compression experiments performed on SNL material were symmetric TiB_2-on-TiB_2 tests. VISAR diagnostics [Barker and Hollenbach, 1972] were used in conjunction with lithium-fluoride windows [Wise and Chhabildas, 1986] to measure time-resolved material interface velocities. This technique has been discussed in detail elsewhere [Kipp and Grady, 1990].

A somewhat different configuration was used in testing the Ernst-Mach (EMI-1) material because of the small sample size available. The sample of TiB_2 ceramic was mounted in a stationary target fixture. A transparent cylinder of lithium-fluoride window material, 19.1-

mm in length and diameter, was bonded to the back of the target ceramic. A laser interferometer (VISAR) was used to measure the time-resolved velocity at the diffused interface between the ceramic and lithium-fluoride window. Planar impact by a copper nosepiece mounted on the projectile caused the propagation of a compressive shock wave through the ceramic sample. The VISAR wave profile measured in this experiment is shown in Figure 1 and compared with a similar profile for SNL-2 material. The pertinent experimental parameters have not been reported elsewhere and are provided in Table 1.

Table 1:
Experimental Parameters for Titanium Diboride (EMI-1) Impact Test

Test Number	Test Material	Target Thickness (ceramic)	Impactor Thickness (copper)	Impact Velocity
		(mm)	(mm)	(km/s)
CE-75	TiB_2	4.521	9.424	1.458

Hugoniot States

As observed in the measured VISAR profile in Figure 1, cusps in the velocity data at about 0.2 km/s and 0.5 km/s for the EMI-1 material clearly identified the upper and lower yields previously observed in other TiB_2 materials. Comparison with SNL material (SNL-2) showed that lower yield for the EMI-1 material was somewhat higher whereas the upper yields for the two materials was comparable.

Hugoniot-stress-versus-specific-volume states were determined from the experimental wave-profile data through assumption of a steady three-wave structure and application of the standard impedance-matching and Hugoniot conservation relations. Hugoniot states for the present test on EMI-1 material are provided in Table 2

Hugoniot data from the present test are compared with similar data in Figure 2. Hugoniots to about 35 GPa for the two SNL materials (SNL-1 and SNL-2) are shown. In addition to the present test on EMI-1 material, which reached a peak stress of approximately 31 GPa, Test S 1065 of Winkler and Stilp (1992) on the same material, reaching a maximum stress of about 14 GPa, is also plotted. The one experiment on EMI-2 material, in which an upper and lower yield was observed (Test S 889), completes the Hugoniot data in Figure 2. A calculated theoretical hydrodynamic curve is also shown in Figure 2 which is based on reasonable ultrasonic and compressibility properties for TiB_2 and provides a basis for examining yield and shear-strength characteristics. The Hugoniot and dynamic strength properties of TiB_2 ceramic plotted in Figure 2 are as follows: The highest density SNL-2 material exhibits a lower yield at about 4-6 GPa and an upper yield near 17 GPa. The somewhat lower density SNL-1 material shows a statistically higher lower yield (6-7 GPa), but the upper yield at approximately 14 GPa is appreciably lower than that of SNL-2. The one experiment on EMI-2 material (Test S 889) exhibits a 4-5 GPa lower yield and

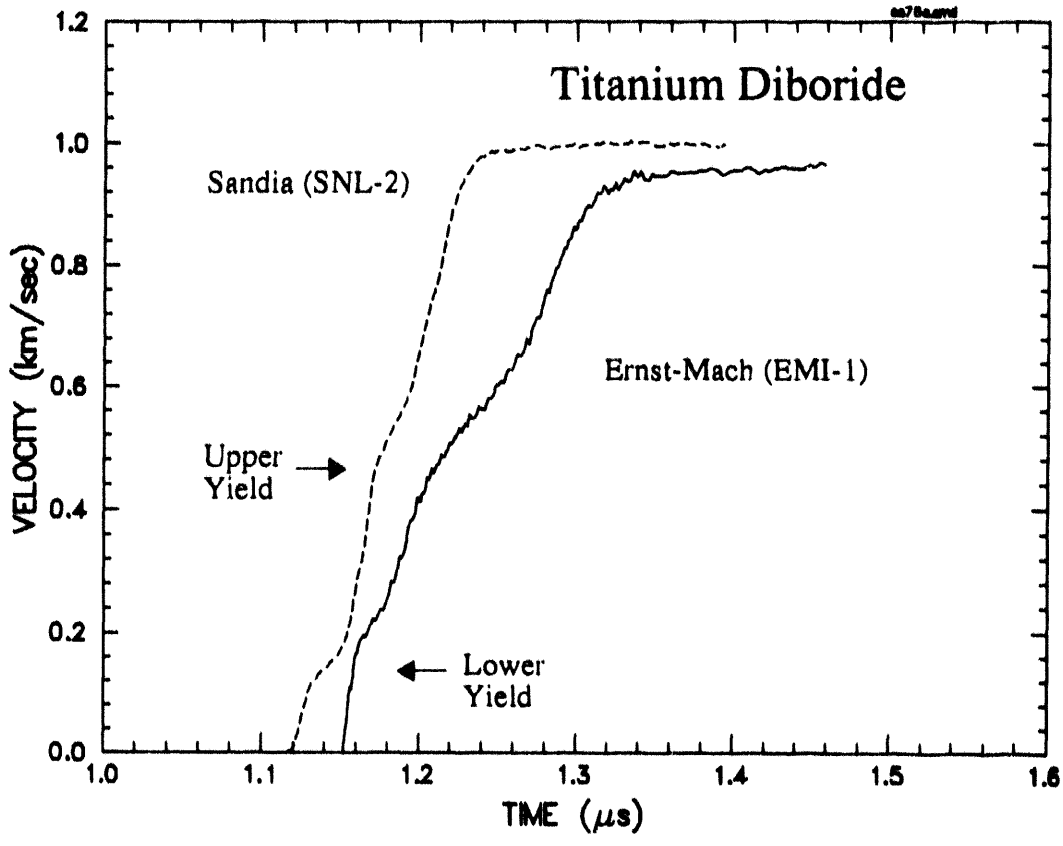

Figure 1. VISAR wave profiles for present experiment on EMI-1 material and earlier SNL material (Peak stress ~ 30 GPa).

about a 9 GPa upper yield. The present SNL test on EMI-1 material to a peak stress of 31 GPa shows, on the other hand, both a lower and an upper yield at approximately 6 and 15 GPa, respectively. Test S 1065, also on EMI-1 material, reached a peak stress of 14 GPa — below the upper yield achieved in the present impact experiment. The higher stress Hugoniot behavior (30-35 GPa) for all materials tends to converge, but not completely. The Hugoniots continue to diverge from the hydrodynamic curve in this range, consistent with recent analysis by Dandekar (1992).

Table 2:
Hugoniot Data for Titanium Diboride (EMI-1) Impact Test

	Shock Velocity	Particle Velocity	Stress	Specific Volume
	(km/s)	(km/s)	(GPa)	(m^3/Mg)
Lower Yield	10.8	0.130	6.15	0.2261
Upper Yield	10.0	0.339	15.28	0.2213
Final State	8.3	0.766	30.74	0.2095

Material Implications

Grain size in TiB_2 ceramic appears to play a secondary role in determining dynamic yield-strength behavior. The lower yield for materials SNL-1 and SNL-2, when considered alone, would appear to be consistent with the frequently applicable Petch relation. However, material EMI-2, which had the smallest grain size, did not have the highest lower yield, and the lower yields for the EMI-1 and EMI-2 materials were reversed from the expected behavior. The upper yields for the four materials were also inconsistent with the common grain-size dependence.

The mechanisms for the double-yield process in TiB_2 ceramic have not yet been established. Winkler and Stilp (1992) have proposed a process of microfracturing at the lower yield, with onset of plastic deformation at the upper yield. Grady (1991) suggested a dual plastic yield process with an initial lower yield which may partially saturate or arrest, followed by onset of pervasive plasticity at the upper-yield level. The possibility of a displacive phase change at the lower-yield level has also not yet been ruled out [Grady, 1992].

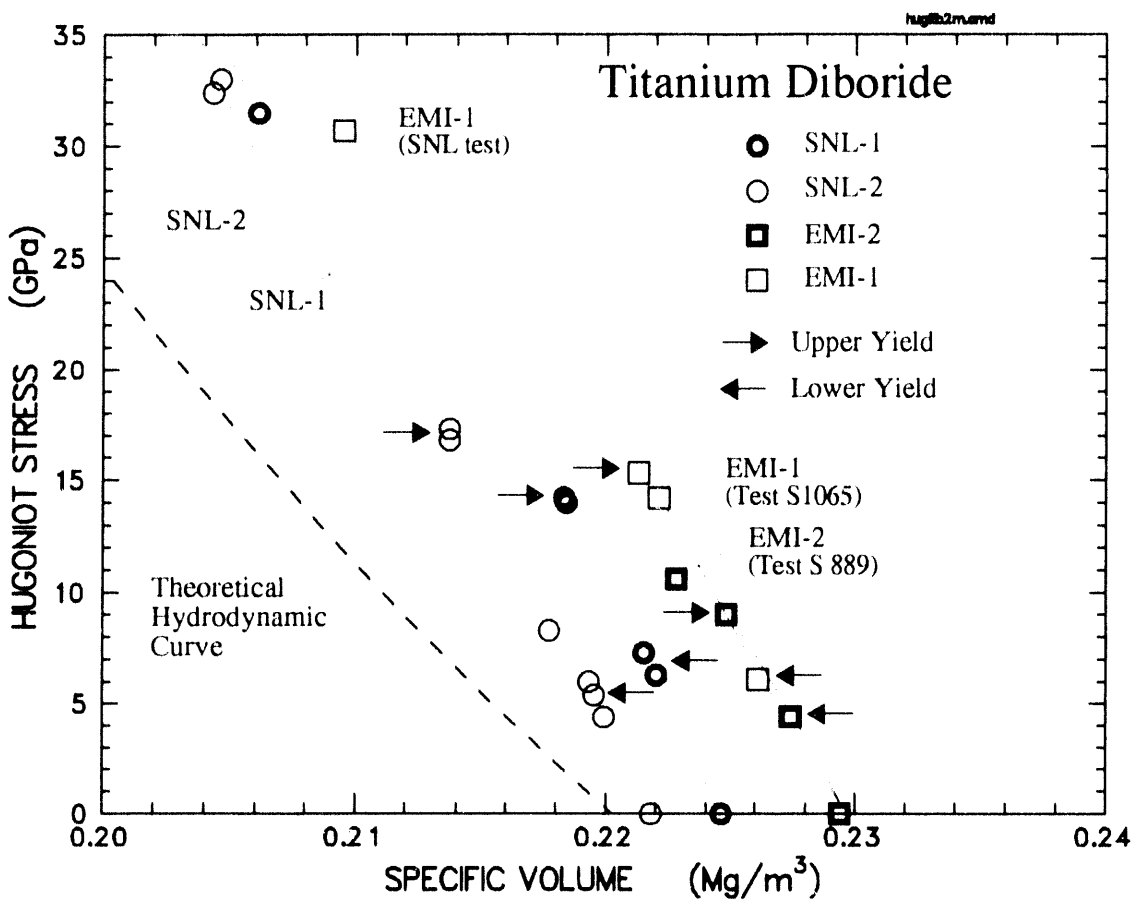

Figure 2. Hugoniot properties of titanium diboride ceramic.

Comparison of the shock-compression behaviors of materials SNL-1, SNL-2, and EMI-2 is of interest. According to the various reported descriptions, the three materials had similar microstructures. Although grain sizes varied somewhat, the porosity consisted primarily of angular voids at grain boundaries and triple grain junctions. The differences in initial densities indicated different levels of porosity in the three materials. Although the issue of impurities sufficient to account for the density differences has not been adequately addressed, this possibility seems less likely. Clearly lower yield is insufficient to collapse porosity in these materials. That this is the case was indicated by the continued separation of the respective stress-volume paths above the 5-7 GPa lower-yield level. The upper-yield behavior was fully consistent with the expected shock-compression response of a ceramic with differing starting porosities. See, for example, the extensive study of Gust, *et al.* (1973) on different aluminum-oxide ceramics. Upper yields of approximately 9, 14, and 17 GPa were consistent with the decreasing starting porosities of these materials. Trajectories of stress-volume paths above the upper yield suggested collapse of porosity and convergence towards a common compression curve.

Within the context of porous materials, the third wave in the profiles shown in Figure 1 can be regarded as a compaction wave. The 8.3 km/s velocity of this wave for the EMI-1 material was about 15% lower than the corresponding wave speed for the SNL-2 material — consistent with the higher porosity of the former. The slow wave speed at the 9 GPa level for Test S 889 reported by Winkler and Stilp (1992) is also consistent with this interpretation.

The shock-compression characteristics of the EMI-1 material provided the anomaly and intriguing exception to the behavior of the other three materials. Based on the large grain size and relatively high porosity of this material, it would be expected to have the lowest strength properties. Comparison of the two wave profiles in Figure 1, however, shows that the upper yield (presumably the onset of pore collapse and pervasive plastic flow) is comparable to the highest strength SNL material. This was unexpected, and was apparently a consequence of the different microstructural characteristics of the porosity in this material. Possibly the predominantly intragranular, spherical-pore structure leads to enhanced strength properties in TiB_2 ceramic. There may be other chemical or microstructural differences that have been overlooked, however.

Summary

Dynamic yield in TiB_2 ceramic is a complex and intriguing phenomenon. The mechanisms responsible for the lower yield process have clearly not yet been identified. Upper yield appears to be consistent with onset of pore collapse and pervasive inelastic shear deformation. Materials SNL-1, SNL-2, and EMI-2, having similar microstructures but different initial porosities, showed a dependence of upper-yield strength on increasing porosity which was fully consistent with commonly observed shock behavior of porous materials. The EMI-1 material, with a different, intracrystalline-porosity microstructure, exhibited unusual enhanced-strength characteristics. The possibility of increased porosity and enhanced strength in ceramics through microstructure manipulation could have important armor-application consequences.

3. Impact Strength and Indentation Hardness of Armor Ceramics

The large dynamic shear strength of certain ceramic compounds is central to the superior armor performance of these materials. Further improvements in strength properties continue to be achieved through improved manufacturing methods and the enhancement of chemical and microstructural features. The dynamic shear behavior is commonly determined through controlled impact methods in which the transient yield strength under loading conditions of uniaxial strain (the Hugoniot elastic limit) is measured. The indentation hardness test is an alternative method for examining strength properties of ceramics which is attractive because of the relatively expedient and cost-effective nature of the experiment. The strength properties of selected ceramics measured by the two test methods are examined in the present work. A degree of correlation between strength data obtained from the two methods is observed and some of the deformation mechanisms which may lead to discrepancies in correlation are discussed. In certain cases the indentation hardness test may provide a useful alternative or complement to the dynamic impact test although there is a need to better understand the deformation processes leading to the strength measurements obtained from the two experimental methods.

Background

There are at least three critical parameters to which the shear strength of a brittle material can be expected to show sensitivity. These are, respectively, the confining pressure, strain rate and size scale. Consideration of these parameters as they relate to the dynamic strength measured in an impact experiment (the Hugoniot elastic limit) and the static strength determined in an indentation hardness test suggests the potential value in the comparison of strength data from the two experimental methods. The Hugoniot elastic limit in an impact experiment is established by the amplitude of the dwell or plateau in a large-amplitude wave structure which has been established over a reasonable propagation distance, and which separates the first elastic wave from the following deformation wave. The Hugoniot elastic limit is usually (although not always) reached through an elastic wave whose risetime is vanishingly small with respect to current wave measurement resolution (1 to 10 ns). The thickness of this first wave, however, does not determine the spacial scale of the material tested for strength in an impact-induced shock-wave experiment. It is the second deformation wave within which the shear strength limit is established, which determines the amplitude of the Hugoniot elastic limit. The deformation wave is usually observed to have a measurable thickness providing that its amplitude is less than a few times that of the elastic wave. The thickness of the deformation wave is strongly dependent on the amplitude of the stress jump through the deformation wave and dimensions of about 10 to 100 μm have been established for the present ceramics when shock loaded to stresses less than 50 GPa. The deformation wave thickness provides the specimen size scale in a shock-wave experiment. This scale compares well with the 10 to 50 μm scale of the region under a hardness indentor.

The state of deformation in a planar-impact shock-wave experiment is one of uniaxial strain. Consequently, when yield is achieved the material is in a high state of confinement.

When the axial stress σ_x achieves the Hugoniot elastic limit, $\sigma_x = \sigma_{hel}$, the lateral stresses are,

$$\sigma_y = \sigma_z = f(\nu)\,\sigma_{hel} \quad , \tag{1}$$

and the mean stress is,

$$p = (\sigma_x + \sigma_y + \sigma_z)/3 = g(\nu)\,\sigma_{hel} \quad , \tag{2}$$

where $f(\nu)$ and $g(\nu)$ are common functions of the Poisson's ratio ν.

The degree of confinement differs starkly from the case of yield under uniaxial stress loading where $\sigma_y = \sigma_z = 0$ and $p = Y/3$ (Y = compressive yield strength). The state of confinement of the material at yield in a static hardness test is more complicated but more closely related to that achieved under planar impact conditions.

Although scale and state of confinement are comparable in the dynamic impact and indentation hardness experiments, the rates of deformation in the two test methods differ by orders of magnitude. Strain rates in a hardness test will be less that 10^{-2}/s, whereas strain rates in the impact tests determined from risetimes of the deformation wave are on the order of 10^5/s to 10^6/s.

Thus, it is argued that strength differences between the shock-wave and indentation hardness measurements is primarily a consequence of strain-rate sensitivities rather than size scale or confining-pressure effects.

Test Methods and Materials

In the present study a dynamic or shock wave measurement of strength is achieved through the use of a propellant gas gun which accelerates a projectile carrying a disc-shaped sample of the ceramic of interest to velocities as high as several kilometers per second. The ceramic sample undergoes planar impact with a similarly-shaped stationary ceramic sample. A thick disc of lithium fluoride is bonded to the back of the stationary ceramic disc and performs as a transparent laser window [Wise and Chhabildas, 1986] for the velocity interferometry (VISAR) system [Barker and Hollenbach, 1972]. The VISAR monitors the time-resolved velocity at the ceramic-lithium fluoride interface, providing a measure of the shock wave profile caused by the high-velocity impact. The amplitude of separation of the two-wave structure in this shock wave measurement determines the dynamic strength or the Hugoniot elastic limit for the material under test.

Indentation hardness measurements were obtained through the Knoop indentation hardness method and were performed by Slavin (1992) at the Army Materials Testing Laboratory.

High strength ceramics tested in the present program were acquired from a number of sources. In several cases the same ceramic obtained from several different suppliers was tested, allowing some comparisons of material property variations due to differences in impurity content, microstructure and ceramic preparation. At present, six different mono-

lithic ceramic materials have been investigated. These are aluminum nitride, aluminum oxide, boron carbide, silicon carbide, titanium diboride and zirconium dioxide. Longitudinal and shear sound velocities, and densities were determined for all ceramics tested. Appropriate data for each ceramic are provided in Table 3. Optical and SEM microstructural examinations have been performed on some of the samples.

The aluminum nitride (AN) under investigation in the present study was acquired from the Dow Chemical Company and is the same ceramic tested in the recent shock-compression studies of Rosenberg, *et al.* (1991). According to the supplier the hot-pressed aluminum nitride tiles have a nominal porosity of 1% and grain size of 2 μm. Ultrasonic and density measurements made in this laboratory indicated a sample-to-sample variation of about 2% in these properties, with the average value reported in Table 3. One aluminum oxide (A1) tested was supplied by the Italian manufacturer Industrie Bitassi. This material contained a significant fraction of glassy phase. The other material (A2) tested was the relatively high-purity Coors AD-995 alumina. Boron carbide from two different suppliers was also tested. The first boron carbide material (B1) was supplied by Eagle Picher Industries. Nominal grain size was 10 μm. The principal contaminant in this ceramic, revealed by electron probe microanalysis, was iron which occurred within voids and other sites distributed quite heterogeneously (relative to the grain size) throughout the material. The second boron carbide (B2) was supplied by Dow Chemical Company. Nominal grain size determined from optical metallography was about 3 μm. The silicon carbide (S1) examined in the study was supplied by Eagle Picher Industries. This ceramic had a nominal grain size of 7 μm and about 1% porosity in the form of spherical cavities on grain boundaries.Titanium diboride from two different suppliers was also tested. The titanium diboride (T1) was supplied by Eagle Picher Industries. A nominal grain size of 12 μm was measured. Both SEM and density measurements indicated several percent porosity in this ceramic. The second titanium diboride (T2) was provided by Cercom Incorporated. This ceramic was higher density and optical microscopy indicated a nominal grain size of about 30 μm. Several types of zirconium dioxide have been studied. The first zirconium dioxide material (Z3) tested was a 12.5 mol% yttria-stabilized cubic zirconia supplied by McDonald Refractory. A nominal grain size of 15 μm was determined, and porosity in this material was approximately 4%. The second zirconium dioxide (Z1 and Z2) was a high quality 3 mol% yttria-stabilized zirconia with nearly 100% tetragonal phase. This material was supplied by Sumimoto Electric Industry in two batches which differed by about 1/2% in initial density. Shock wave properties for these zirconia materials are reported in Grady and Mashimo (1992). Shock wave properties of the other ceramics are discussed in Grady (1991, 1992).

Results and Discussion

Results of the static indentation measurements and the impact Hugoniot elastic limit measurements for the ceramics tested are provided in Table 3. An equivalent dynamic yield strength is determined through the relation

$$Y_d = 2\frac{C_s^2}{C_l^2}\sigma_{hel} \quad , \tag{3}$$

where C_s and C_l are the shear and longitudinal sound velocities and where constant elastic properties are assumed for the materials within the yield surface.

Table 3:
Indentation Hardness and Dynamic Strength Data

Material	Code[a]	Density	C_l	C_s	Dynamic Yield[b]	Hardness
		(kg/m^3)	(km/s)	(km/s)	(GPa)	(GPa)
AlN	AN	3254	10.73	6.32	5.5	10.6
Al_2O_3	A1	3555	9.28	5.47	3.6	10.6
Al_2O_3	A2	3890	10.56	6.24	4.3	14.5
B_4C	B1	2517	14.04	8.90	13.7	26.2
B_4C	B2	2506	14.07	8.87	15.1	25.6
SiC	S1	3177	12.06	7.67	12.5	22.3
TiB_2	T1	4452	10.93	7.30	11.6(5.4)	19.0
TiB_2	T2	4509	10.79	7.43	15.2(3.8)	19.6
ZrO_2	Z1	5602	6.61	3.54	3.2	8.5
ZrO_2	Z2	6028	7.11	3.72	8.9	11.4
ZrO_2	Z3	5954	6.87	3.63	7.4	10.7

(a) Code is identified in the text.
(b) Numbers in parentheses are lower yield for TiB_2 (see text).

The dynamic yield and hardness measurements are correlated in Figure 3. It is instructive to compare the data to earlier results [Cline, 1989; Gilman, 1970] in which some of the same ceramics were investigated. A noticeable difference is the somewhat weaker correlation of static and dynamic strength observed in the more recent data. The general trend, however, is similar with a slope of unity and the magnitude of dynamic yield of order one-half of the static hardness.

The spread in dynamic strength values of some of the materials is due to the sensitivity of the VISAR diagnostic to initial yield in the porous samples (about 1% to 2% in most of the ceramics). The first break in the elastic wave profile associated with the Hugoniot elastic limit will differ markedly for the same ceramic for variations only in initial porosity. It is expected, however, that subsequent or post-yield strength hardening occurs as inelastic pore collapse proceeds during the shock-compression process. It is suspected that the indentation hardness test is less sensitive to yield onset and provides a strength measurement which averages over a larger deformation strain. Consequently, the indentation hardness

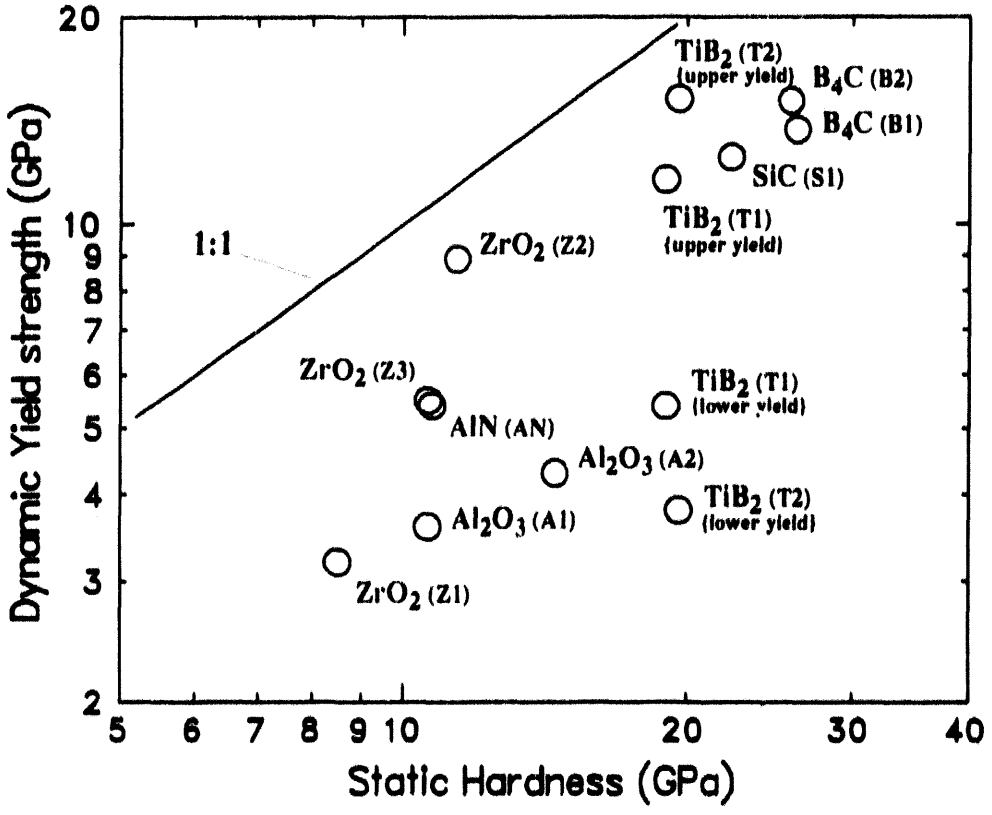

Figure 3. Correlation of dynamic strength and indentation hardness for selected ceramics.

measurement would be less sensitive to moderate variations in porosity in a specific ceramic.

This difference in sensitivities of the two test methods appears to explain the strength measurements for the two tetragonal zirconia samples which differed only in initial porosity, and probably explains the two titanium diboride points (upper yield) whose density difference is most likely also related to a small porosity difference. As seen in Figure 3, the dynamic strength for these two materials is observed to depend sensitively on the variations in porosity whereas indentation hardness measurements are relatively insensitive to these same variations. The dynamic yield for the two aluminum oxides and the cubic zirconium dioxide, which seem to be below the general trend of the data may also be related to the excessive porosity in these materials. The larger glassy component in the Bitassi alumina probably accounts for the significant reduction in indentation hardness compared to that of Coors AD-995 alumina.

Titanium diboride is unusual in that time-resolved controlled impact experiments indicate a complex two-step yield process for this material (Grady, 1992). The shock data suggests a secondary nonpervasive yield at about 4 to 5 GPa shear stress which quickly saturates and is followed by onset of pervasive shear yield at about 12 to 15 GPa. It is interesting to note in Figure 3 that indentation hardness and dynamic yield for this material correlates with the general trend of the data if the upper yield is considered.

Impact experiments on boron carbide identify a high initial dynamic shear strength as is shown in Figure 3, but dramatic shear strength softening occurs with subsequent deformation. This behavior has not been observed in the other ceramics tested. The comparatively high indentation hardness measurements for boron carbide do not reflect this softening, suggesting that it is strictly a dynamic effect — possibly local thermal softening or a lattice instability in the boron carbide structure.

Summary

It can be argued that shock compression and indentation hardness methods test the strength characteristics of material under similar states of confining pressure and of similar size scale, differing principally in the rate of loading. Comparisons of shock wave and indentation hardness measurements show a reasonable correlation in strength values between the two test methods. Nominal agreement in magnitude suggests that strain rate effects in these ceramic may be weak. It is also suggested that differing sensitivities of the two test methods to modest variations in initial porosity may account for much of the correlation scatter. It is suggested that indentation hardness tests average over larger strains, providing a strength measure closer to that of the fully dense material. In contrast, the high resolution of the shock-wave VISAR diagnostic leads to more detailed information on porosity sensitivity and deformation hardening. Improved understanding of deformation details in the two test methods should lead to enhanced material strength data for computational model development and application.

4. Hydrodynamic Equation of State of Silicon Carbide Through Shock Compression Experiments on Metal-Ceramic Mixtures

Planar shock-compression experiments on monolithic ceramics provide measurements of axial-stress and specific-volume states commensurate with the high-strain-rate, large-confining-pressure environment of an impact test. The large shear stresses achieved during the uniaxial-strain compression process are evidenced by the Hugoniot elastic limit — an onset of softening in the axial-stress-versus-specific-volume response due to inelastic yielding in shear. Unless both longitudinal and transverse stress are measured in the shock compression experiment, complete deviatoric-stress constitutive data required to fully model the dynamic compression and flow process are not provided by the experiment. Although transverse stress measurements within the shock environment have been performed, the methods are still developmental and results in many cases are not fully satisfactory.

An alternative method commonly used to infer the deviatoric constitutive properties of the material during the shock compression process is to relate the Hugoniot or longitudinal stress versus specific-volume curve to the hydrodynamic response of the material. The latter is usually determined by the correction of isothermal hydrostatic data for adiabatic conditions within the shock process, or by extrapolation of lower pressure ultrasonic data using accepted functional forms for the higher pressure compression behavior.

Another method, and that which is pursued here, is to directly measure the hydrodynamic compression of the material of interest through shock-wave techniques. The method involves the immersion or mixing of the test material into a matrix material which is fluid-like in its shock-compression behavior (i.e., unable to support deviatoric stresses). This approach was originally explored by Adadurov, *et al.* (1962). It was used by Kanel' and Pityulin (1984) to measure the hydrodynamic properties of titanium carbide. More recently, Tang and Gupta (1988) used the technique to investigate phase transformation in cadmium sulfide, and Poderetz, *et al.* (1988) have investigated the dynamic compression of silicon dioxide using similar methods.

In the present study we investigate the hydrodynamic response of silicon carbide to approximately 30 GPa through shock-compression studies on mixtures of silicon carbide and copper prepared by hot compaction methods. Relative to the large strength properties of silicon carbide, the low yield properties of copper are expected to result in shock compressed states in the mixture with sensibly low values of deviatoric stress.

Material Preparation

Mixture samples were prepared from powders of α-silicon carbide and copper. Nominal grain size of the silicon carbide was 15-20 μm and the particle distribution was fairly narrow. Minus-325 mesh, three-nines purity copper was used as the matrix material. To achieve the 50%-50% volume mixture, based on crystal densities of 3220 kg/m^3 for SiC and 8920 kg/m^3 for Cu, 16.26 g of SiC and 45.05 g of Cu were combined.

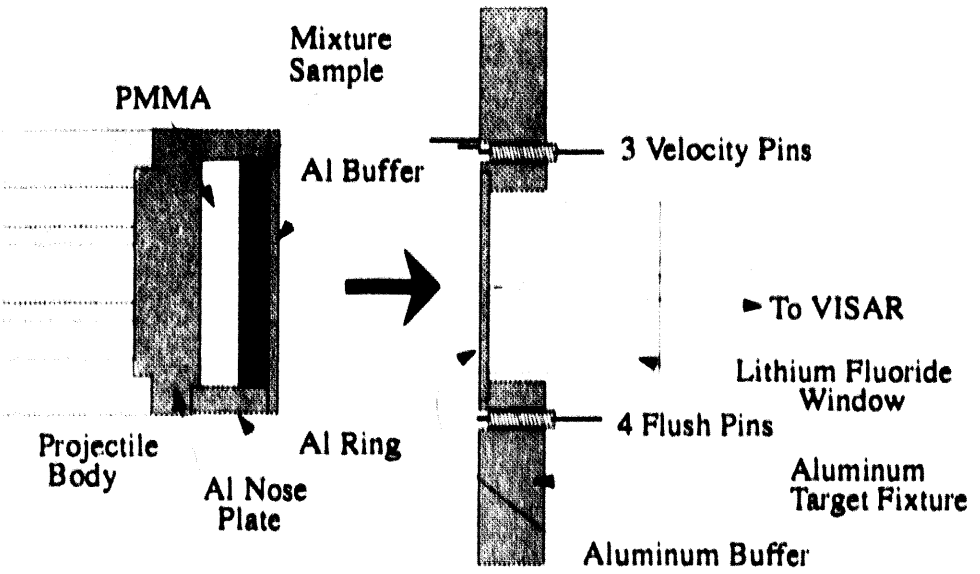

Figure 4. Experimental configuration for Hugoniot and release tests.

A set of six samples were prepared with hot-pressing techniques in the form of uniform discs which after machining were approximately 5 mm in thickness and 38 mm in diameter. One sample was sectioned and polished. Optical metallographs indicated a uniform distribution of SiC particles throughout the sample. Ultrasound tests and low densities, however, indicated extensive central cracking due to cooling stresses in several specimens. Two samples from this batch were judged acceptable with densities of 5830 and 5840 kg/m^3, respectively. Comparison with a theoretical density of 6070 kg/m^3 for a 50%-50% mixture suggests several percent porosity. A second batch of three further samples were prepared with slight variations in the temperature-pressure history during fabrication. All samples from this batch appeared acceptable by ultrasound scan and density measurements. Densities were close to 5990 kg/m^3. Shock wave experiments were performed on the two acceptable samples from the first batch and on two samples from the second batch.

Measured longitudinal and shear ultrasonic velocities were 5260 m/s and 3250 m/s, respectively. Statistically significant differences between the two batches were not observed.

Shock Compression Methods

Shock-compression experiments were performed to measure both Hugoniot and release states in the metal-ceramic composite samples. The method used incorporated laser interferometry shock-wave diagnostics and was developed specifically for accurate Hugoniot and release state analysis [Grady and Furnish, 1988]. The experimental assembly is illustrated in Figure 4. The mixture sample is mounted on the projectile, backed by PMMA (polymethylmethacrylate) and preceded by a thin disc of aluminum (6061-T6 alloy). The stationary target consists of a thin aluminum disc followed by a lithium fluoride window

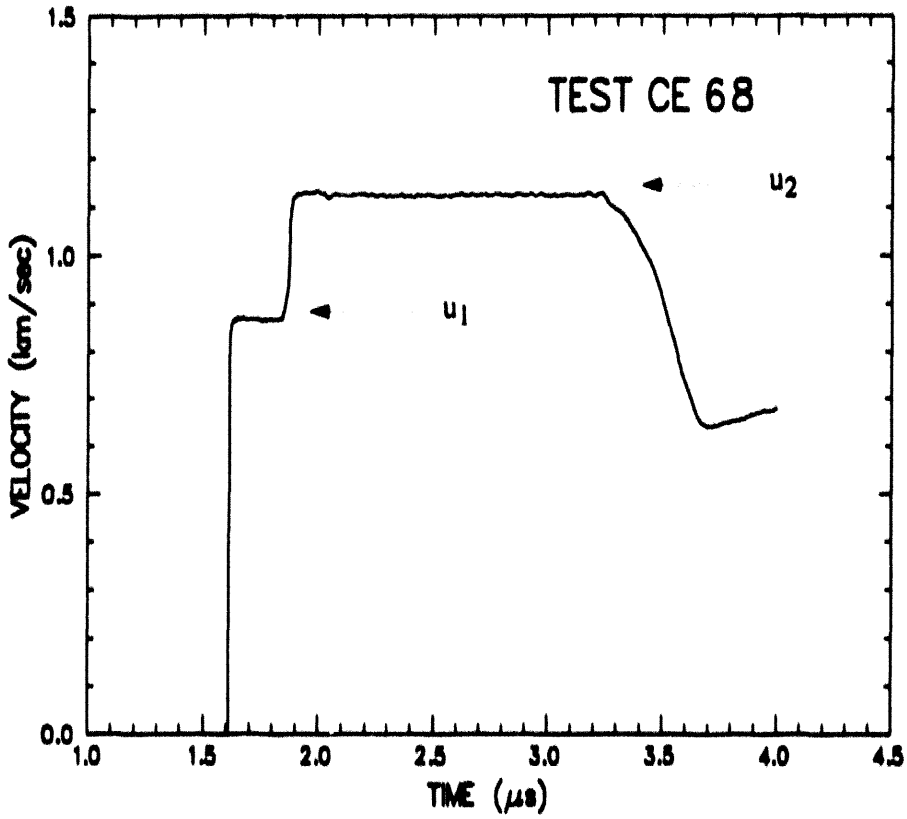

Figure 5. Interface particle-velocity profile for test CE-68.

material [Wise and Chhabildas, 1986]. As noted earlier, specimen discs were approximately 38 mm in diameter. Specimen thicknesses are provided in Table 4.

Projectiles were accelerated to velocities between 1.0-2.4 km/s with a single-stage propellant gun and underwent planar impact with the target. Diffused-surface velocity interferometry or VISAR [Barker and Hollenbach, 1972] was used to monitor the time-resolved velocity at the aluminum-LiF interface in the target. A representative motion history for one of the present tests is shown in Figure 5. Peripheral electrical shorting pins are used to measure projectile velocity and planarity of impact (see Figure 4).

Impact velocities were selected to achieve Hugoniot pressures over the range 15-30 GPa in approximately 5 GPa increments. The maximum velocity achievable (~2.38 km/s) with the propellant gun facility was necessary to attain the 30 GPa Hugoniot pressure point. Necessary experimental and Hugoniot properties are provided in Table 4

Mixture analysis

To calculate the hydrodynamic compressibility of silicon carbide from the Hugoniot measurements on the mixture, some simplifying assumptions are needed. First, it is assumed that any initial porosity is collapsed and eliminated during the shock compression process. Further, based on the relatively low yield stress of the copper matrix it is assumed that stress deviators in the mixture at the shock state are sufficiently low that the measured

Hugoniot stress can be sensibly equated to the pressure. Finally, it is assumed that the compressibility of silicon carbide and copper are additive. That is,

$$\upsilon(p) = \lambda \upsilon_1(p) + (1-\lambda)\,\upsilon_2(p) \quad , \tag{4}$$

where υ, υ_1 and υ_2 are the specific volumes of the mixture, silicon carbide and copper, respectively, and λ is the mass fraction of silicon carbide in the mixture.

Based on a 50%-50% volume ratio of silicon carbide and copper, the mass fraction of silicon carbide is calculated to be $\lambda = 0.265$. The compressibility of copper is calculated from its known Hugoniot properties. Linear shock-velocity versus particle-velocity parameters for copper [Marsh, 1980] are $C = 3.940$ km/s and $S = 1.49$. The compressibility of silicon carbide calculated from Equation 4 is plotted in Figure 6. Horizontal error bars shown for the four data points are determined by the uncertainty in Hugoniot response of the mixture and due in turn to the uncertainty in initial mass fraction of components. Also shown is the Hugoniot for monolithic silicon carbide [Kipp and Grady, 1989]. Analytic estimates of the hydrodynamic response in Figure 6 identified by the dashed lines are based on the theoretical density of silicon carbide, a bulk modulus calculated from ultrasonic data, and extrapolation to high pressures with a linear shock-velocity versus particle-velocity expression where $S = 0.8$ and 1.2, respectively, and $C = 8190$ m/s . A value of S near unity is consistent with the high-pressure Hugoniot data for silicon carbide from Gust, *et al.* (1973). Also shown are static compressibility measurements of Bassett and Weathers [Holmquist, 1991] using diamond anvil technology..

Table 4:
Hugoniot Experiments

Test No.	Sample dens.	Impact vel.	Sample thk.	Proj. al thk.	Targ. al thk.	Hug. press.	Hug. part. vel.	Hug. spec. vol.
	(kg/m^3)	(km/s)	(mm)	(mm)	(mm)	(GPa)	(km/s)	($m^3/kg \times 10^6$)
CE-68	5930	1.728	5.01	1.05	1.02	19.9	0.578	151.7
CE-69	5940	2.361	5.01	1.05	1.02	29.7	0.840	144.7
CE-78	5991	2.027	4.98	1.05	1.00	24.5	0.715	146.2
CE-79	5989	1.275	4.97	1.05	1.01	14.1	0.422	154.4

Discussion

The compression states determined from the present mixture experiments and shown in Figure 6 are somewhat surprising. It is difficult to accept the data at 14 GPa and perhaps even that at 20 GPa as representative of the hydrodynamic compressibility of silicon carbide. Extrapolation of ultrasonic data to these pressures could not be too far wrong. Ultrasonic measurements were obtained on silicon carbide ceramic samples which were a few

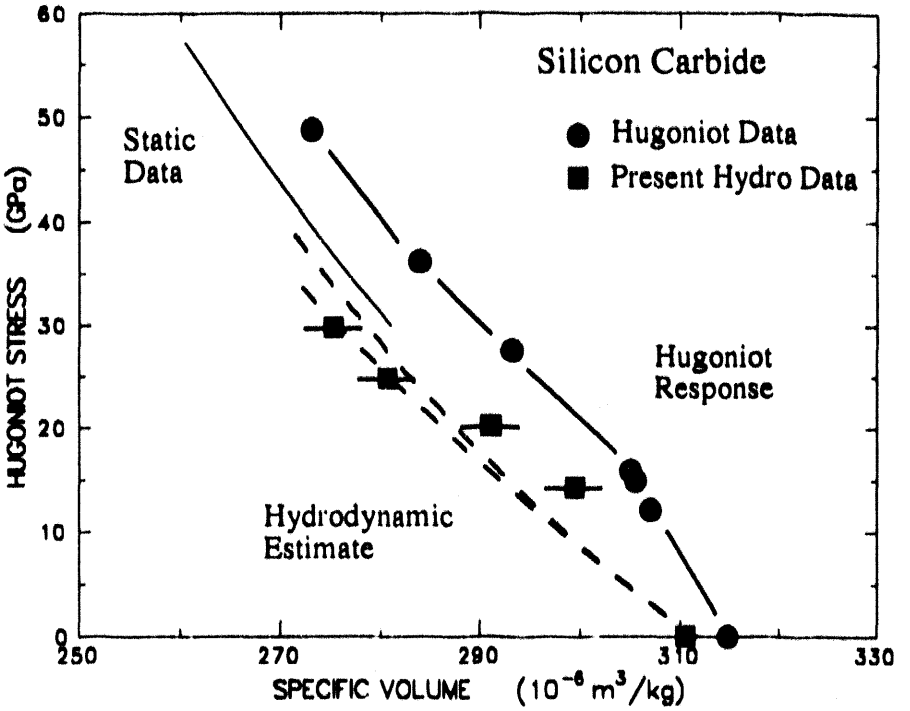

Figure 6. Compressibility of silicon carbide based on mixture Hugoniot measurements and analysis. Static data from Holmquist (1991).

percent porous. Hence the theoretical density bulk modulus would be somewhat higher but certainly not by more than about 5%.

Thus, it appears that strength effects in the mixture Hugoniot experiments at these lower pressure levels compromise the assumed hydrodynamic behavior. Strength effects at these pressures are somewhat unexpected due to the low flow stress (0.1-0.2 GPa) of copper. There are several possible strength issues which could cause the difficulty. The samples are several percent porous and if the shock compression process is not sufficient to remove this porosity then calculated compressions would be in error. This behavior might occur for example if the micrometer scale motions and large local deformations necessary to collapse the voids led to enhanced flow stress in the copper. Secondly, the mixture matrix as a whole at these stress states may be supporting deviatoric stresses. Stress differences might be experienced if sufficient bridging between silicon carbide particles occurred to allow the strength of the ceramic to be felt. Although the copper is somewhat more compressible than the silicon carbide, the overall strain levels are sufficiently modest that the extent of particle contact will not differ significantly from that observed in the pretest micrographs. Resistance to pore collapse and enhanced copper strength would seem to be the more likely explanation for the indicated strength behavior for the experiments at Hugoniot stress levels below about 20 GPa.

The two experiments achieving Hugoniot stresses in excess of 20 GPa appear to be providing reasonable estimates of the hydrodynamic compressibility of silicon carbide (Figure 6). The error bars are conservative in light of the uncertainty in silicon carbide content

in the present materials. Possible strength contributions would shift the hydrodynamic states even further to the left. These data points are in reasonable agreement with the extrapolated hydrodynamic curves based on ultrasonic properties. They lie somewhat to the left of the static data of Bassett and Weathers [Holmquist, 1991].

The observed compression and release behavior of all of the data could also be explained by a phase transition in silicon carbide although this possibility seems unlikely. Gust, *et al.* (1973) have suggested a shock-induced phase change in silicon carbide within this range from observations on shock data. Compressive shock profile measurements of Kipp and Grady (1990) do not show evidence for a phase transition although the nondispersive character of release waves could imply reversion from a high-pressure phase. Examination of silicon carbide samples shocked to as high as 80 GPa [Kovtun and Timofeeva, 1988] did not reveal quenched high-pressure phases. The static compression study of Basset and Weathers [Holmquist, 1991] on α-silicon carbide does not indicate a high-pressure transition.

5. Development of Extended Dynamic Pressure-Shear Testing Methods

A new impact-test configuration has been developed and demonstrated which permits time-resolved investigations of the dynamic response of materials in a multiaxial-strain environment. Like the rod test described by Taylor [1948], this technique involved the impact of a cylindrical, flat-ended rod of test material with an anvil. However, innovations incorporated in the present test arrangement yielded significant material-response information that is not provided by a traditional Taylor test.

With Taylor's approach, a free-flying test rod impacts a stationary, "rigid" anvil, and post-test observation of the position of the boundary between unstrained and plastically-deformed regions of the rod yields an estimate for the dynamic, compressive yield strength of the rod material. This estimate relies on simplifying assumptions regarding the motion of the elastic/plastic boundary from the impact end of the rod to its final, measured (post-test) location in the rod. Taylor's method ignores the effects of radial inertia, and requires intact recovery of the rod.

With the present method, the *anvil* was launched, and it struck an initially stationary, flat-ended rod of test material. This rod was either free (unconfined), or mounted within a close-fitting confinement sleeve, thereby allowing adjustment of the level of lateral confinement. Velocity interferometer diagnostics [Barker and Hollenbach, 1972] provided measurements of the axial (longitudinal) free-surface velocity history of the free end of the rod, and of the transverse (radial) velocity for one or more points on the periphery of the target rod or confinement sleeve. Subsequent analysis of the resultant velocity records, which did not rely on simplifying assumptions regarding the rod deformation, allowed assessment of dynamic material properties, such as wave speeds and compressive yield strength, without the requirement for intact recovery of the rod. This feature made the present technique particularly attractive for studies of brittle ceramics which are inherently unsuitable for evaluation with the traditional Taylor method since they invariably fragment for impact stresses in excess of the yield strength.

Experimental Configuration

The test geometry for impact studies on confined and unconfined ceramic rods is illustrated in Figure 7. For all experiments conducted to date, the ceramic rod was fabricated from Coors AD-995 alumina, and was produced with a final nominal diameter of 10 mm. For experiments involving no confinement, the ceramic rod was mounted directly within a low-density foam collar which, in turn, was held by an aluminum support ring. For the confined tests, the ceramic rod was first installed in a close-fitting metallic sleeve with a nominal outer diameter of 20 mm, then this sleeve was mounted within the foam collar. The foam effectively decoupled the rod or sleeve from the high stresses produced in the support ring by projectile impact.

Dynamic loading of the ceramic rod or rod/sleeve assembly was produced by a flat-faced projectile which was launched by the powder gun. The monolithic impactor, or anvil, was fabricated from 6061-T6 aluminum, and featured (1) a forward flat-plate section that was

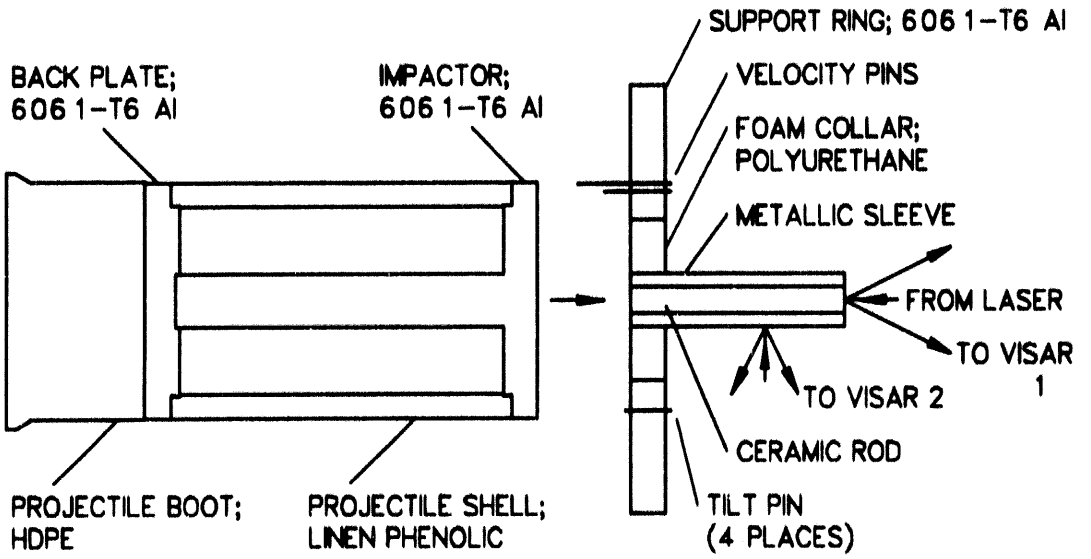

Figure 7. Experimental configuration for observations of dynamic, multiaxial response of ceramic rods.

nearly full bore diameter and nominally 12.7-mm thick, and (2) a trailing rod section that was nominally 20-mm diameter and 122-mm long. This rod section was incorporated as a means of maximizing the duration of high stress at the impact end of the target rod. Coaxial shorting pins mounted around the support-ring periphery were struck by the plate section of the impactor and generated signals which permitted determination of impact velocity and tilt.

Several parameters were varied during testing with the present experimental configuration. The level of rod confinement was altered by using either *no* sleeve, or a ductile, high-shock-impedance metallic sleeve machined from either tantalum (Ta) or OFHC (oxygen-free, high-conductivity) copper. Other parameters which were changed included the rod length-to-diameter ratio (L/D = 4 or 8), and the impact velocity (nominally either 1.1 or 2.1 km/s). The selected impact velocities produced peak stresses in the ceramic rod of either 2 or 4 times the 6.16-GPa Hugoniot elastic limit which has been measured for Coors AD-995 alumina in recent tests at SNL (see Section 3).

Free-surface Velocity Measurements

During each experiment, time-resolved particle velocity data were acquired *simultaneously* at two or more locations: one VISAR monitored the longitudinal (axial) velocity at a point coincident with the center of the rod's free face, and each remaining interferometer monitored the transverse (radial) velocity for a preselected measurement point which was positioned several rod diameters from the initial impact plane on the curved outer surface of the rod or confinement sleeve (when present).

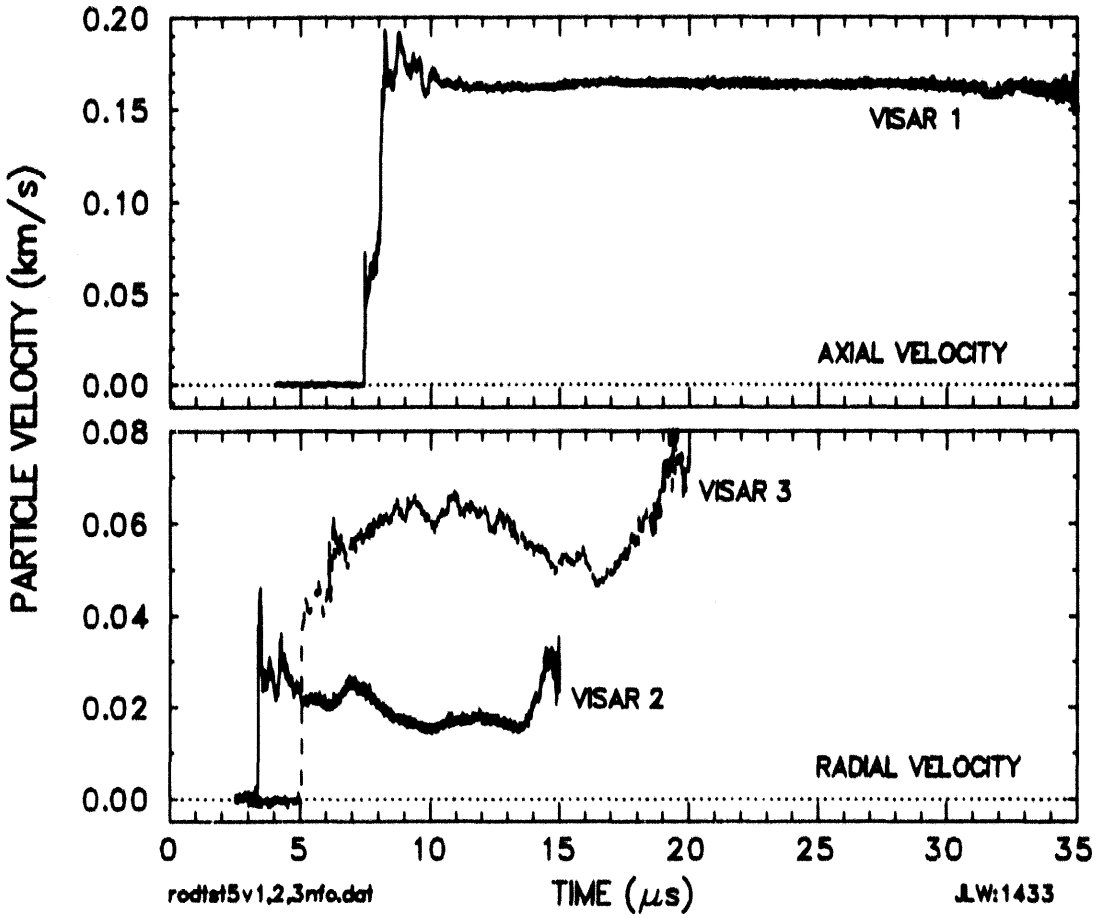

Figure 8. Axial (upper trace) and radial (lower traces) free-surface velocity data for shot RODTST5 (no confinement sleeve).

Representative velocity records are displayed in Figures 8 and 9, respectively, for experiments RODTST5 and RODTST6. In each of these tests, a 10-mm diameter by 80-mm long (L/D = 8) alumina rod was impacted at about 1.1 km/s. No metallic confinement sleeve was used for RODTST5, whereas a tantalum sleeve (20-mm outer diameter) was used for RODTST6. In both experiments, axial velocity data were successfully recorded by VISAR 1 during a time interval extending at least 25 μs after first detectable motion. Qualitatively, the axial-velocity records were characterized by the arrival of an initial elastic compression (which propagated at about the ultrasonic longitudinal velocity, C_l = 10.6 km/s), followed by a second compressional wave (travelling at about the bar velocity, C_b = 9.81 km/s) that brought the velocity to its peak value. The axial velocity subsequently decayed only slightly from this peak (~ 10% - 20%, respectively, for RODTST5 and 6), then attained an essentially constant equilibrium value which persisted for the duration of the recording time.

Radial velocity data were also successfully acquired during experiments RODTST5 and 6 using two interferometers, VISAR 2 and 3, whose measurement points were positioned,

respectively, 30 and 50 mm from the initial impact plane. In both tests, the recording interval following first detectable motion for the radial-velocity data was about 9 -12 μs for VISAR 2 and about 12 -15 μs for VISAR 3. For the unconfined rod (test 5), the radial-velocity records indicated a similar amplitude (~0.047 km/s) for the first peak, but divergent behavior thereafter with the downstream recording station (VISAR 3) displaying significantly higher velocities. These differences were most likely related to nonuniform failure of the ceramic. For the confined rod (test 6), the two radial-velocity records indicated mutually consistent structure and amplitudes with the downstream record (VISAR 3) displaying evidence of geometric attenuation effects at early times.The observed negative values of radial velocity (detected by both VISAR 2 and 3) for times in the 9 -15 μs interval were qualitatively and quantitatively consistent with pretest two-dimensional simulations made by Swegle [1992] using the ARTOO wavecode [Swegle, 1981].

Yield strength Estimates

As noted above, the axial velocity observed at the free end of the rod reached an equilibrium value shortly after arrival of the second major compressional wave (which had propagated through the rod at approximately the bar velocity). Referring to Figure 10, the

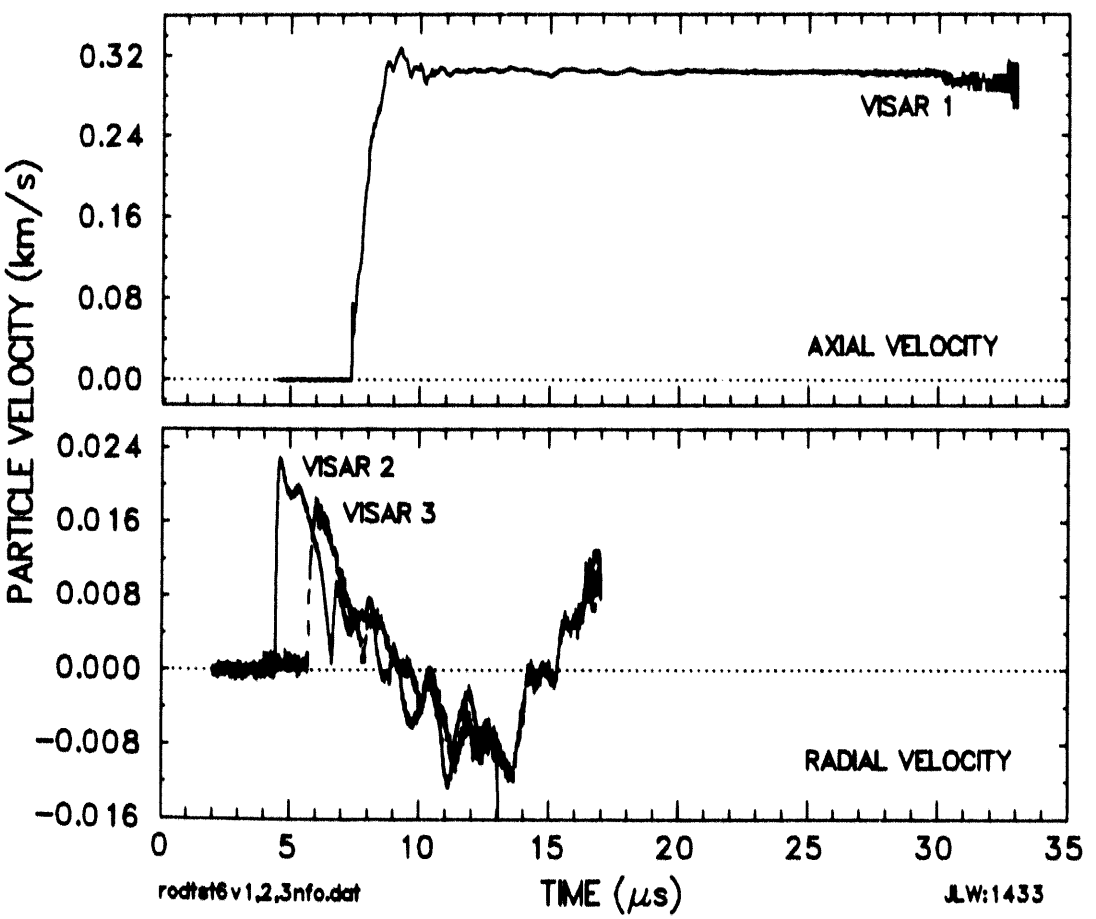

Figure 9. Axial (upper trace) and radial (lower traces) free-surface velocity data for shot RODTST6 (Ta confinement sleeve).

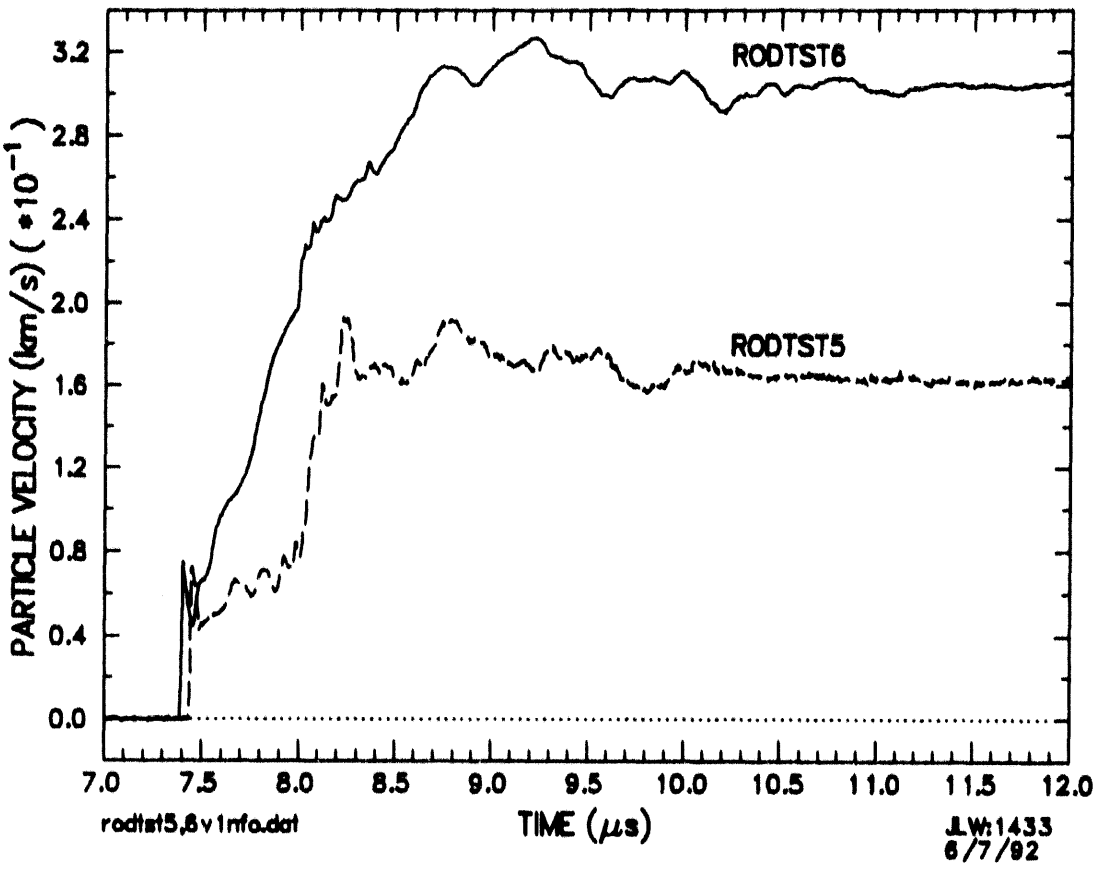

Figure 10. Comparison of axial (longitudinal) free-surface velocity histories for shots RODTST5 (no sleeve) and RODTST6 (Ta sleeve).

amplitude of this equilibrium velocity was dependent on the level of lateral confinement. For shot RODTST5, no confinement sleeve was used, and the equilibrium free-surface axial velocity, designated u_{eq}, was 0.165 km/s. For shot RODTST6, a Ta sleeve was used, and the resultant value of u_{eq} was 0.304 km/s.

Using the measured value of u_{eq} for a given test, the corresponding *in situ* axial stress achieved through the incident bar wave, σ_{xh}, was estimated from the relation,

$$\sigma_{xh} \approx \frac{1}{2}\rho_0 C_b u_{eq} \quad , \tag{5}$$

where ρ_0 and C_b were, respectively, the initial density (3890 kg/m^3) and bar velocity of the rod material. On this basis, a value of $\sigma_{xh} = 3.15$ GPa was obtained for shot RODTST5 (no confinement), whereas $\sigma_{xh} = 5.80$ GPa was obtained for shot RODTST6 (Ta confinement). This increase in stress-wave amplitude with increased confinement was consistent with expectations of an upper dynamic limit of $\sigma_x = \sigma_{Hel} = 6.16$ GPa for the case of rigid confinement (*i.e.*, uniaxial strain). The axial stress supported by the Ta-confined rod (5.80 GPa) closely approached this limiting value. On the other hand, the unconfined rod (test 5) supported a dynamic axial stress which was significantly lower than the

Hugoniot elastic limit; in this case, conditions in the rod closely approximated a state of uniaxial-stress ($\sigma_y = \sigma_t = 0$), and, as expected, the yield strength of the material was diminished. In comparison, the observed stress value of $\sigma_{xh} = 3.15$ GPa for the unconfined rod was significantly lower than the predicted value of $\sigma_x = Y_d = 4.3$ GPa (where Y_d = dynamic yield strength; see Table 3). This result suggested that surface effects play an important role in determining the yield strength of *unconfined* ceramic material.

6. Hugoniot and Dynamic Tensile Strength Experiments on High-Quality Aluminum Oxide

Several controlled-impact strength experiments were performed on a high-quality aluminum oxide ceramic provided by the Michigan Technological University in support of materials development research at that facility [Staehler, *et al.*, 1991]. In one test the impact amplitude just exceeded the dynamic uniaxial strain yield strength (HEL) of the ceramic. In the second test peak stresses approximately three times the HEL were achieved. Experiments were designed such that tensile spall of the ceramic specimens was achieved on stress unloading. Supporting shock recovery experiments were also performed.

Background

Because of the early and wide availability of good quality aluminum oxide ceramic and single crystal aluminum oxide, shock Hugoniot equation-of-state measurements on this material have been extensive. Sapphire, which is the Al_2O_3 single crystal form, has a rhombohedral hexagonal crystal structure with close-packed oxygen ions. Early Hugoniot equation-of-state studies on single-crystal and polycrystalline aluminum oxide includes the work of McQueen and Marsh (1960) and Ahrens, *et al.* (1968) to nearly 150 GPa, and the investigation of Brooks and Graham (1971) which included a determination of Hugoniot elastic limit dependence on crystal orientation in single crystal Al_2O_3. No phase transitions have been observed in this material under shock or static loading to pressures in excess of 100 GPa. A useful summary of this early shock data is included in the recent work of Mashimo, *et al.* (1988).

The extensive shock-wave investigation of aluminum oxide by Gust and Royce (1971) is also noteworthy. Shock Hugoniot and strength data for 4 aluminum oxide ceramics ranging in porosity from about 6% to near theoretical density were provided to nearly 100 GPa. HEL strengths ranging from 6-13 GPa were reported although a marked dependence of HEL value on sample thickness was noted. Analysis of the dynamic porosity crush process indicated a quadratic crush curve, with crush complete at about 30 GPa (3-5 times the initial HEL).

The research of Cagnoux and Longy (1988) and Yeshurin, *et al.* (1988) on the shock deformation properties of aluminum oxide ceramic should also be noted. Both studies address the effect of microstructure on dynamic yield and strength, identifying microstructural heterogeneity (coarse grain structure or dissimilar second phases) as critical to the mode of failure. Homogeneous fine-grain aluminum oxide yields through dislocation plasticity, whereas heterogeneous material undergoes pervasive microcracking due to local tensile stresses in the dynamic failure process. Cagnoux and Longy (1988) observed no strain rate dependence of the Hugoniot elastic limit in aluminum oxide ceramic over the range of about 5×10^5/s to 5×10^6/s.

Velocity interferometry measurements of compression and release wave behavior for fully dense aluminum oxide have been performed by Munson and Lawrence (1979) to 16 GPa. Within this stress range (the measured HEL for the material studied was 9.1 GPa) the de-

formation wave is dispersive, presumably due to viscous effects brought about by kinetics of the yield process. Release is reported to be fully elastic within this range. Dynamic yield was attributed to pervasive microfracturing. The latter conclusion was based on the observed lack of spall strength measured on release.

In the present study we provide several additional compression and release wave profiles on the high-quality aluminum oxide ceramic provided by Michigan Technological University. Maximum compression states are approximately 36 GPa. Dynamic compressive strength and release properties are examined in light of the new data.

Material

The present aluminum oxide samples were prepared by hot isostatic pressing of 99.99% pure aluminum oxide powder [Staehler, *et al.*, 1991]. No additives of any kind were included, thus minimizing the formation of second phases. A mean grain diameter of slightly under one micrometer was achieved. Samples achieved a near-theoretical density of 3970 kg/m^3. The measured longitudinal and shear wave speeds were 10.91 km/s and 6.44 km/s, respectively.

Experiment

The configuration for the controlled-impact shock-wave experiments is shown in Figure 11. Samples of the aluminum oxide ceramic were mounted in both the target and the projectile. A transparent disc of lithium fluoride window material 19.1 mm in thickness and

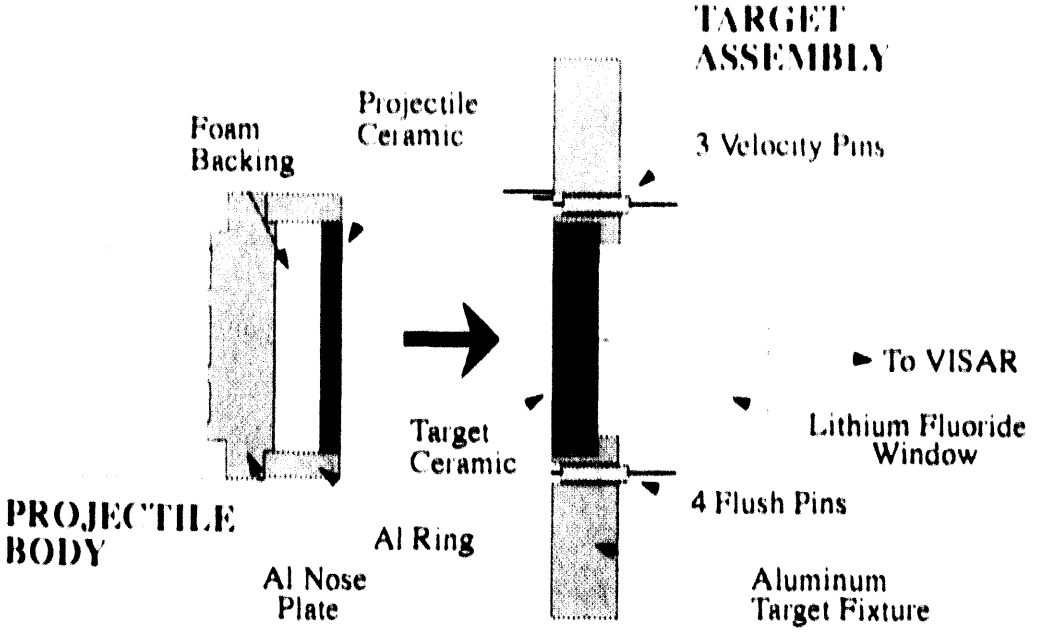

Figure 11. Experimental configuration for shock and release experiment on aluminum oxide ceramic

25.4 mm in diameter was bonded to the back of the stationary target ceramic. A diffused-surface laser interferometer (VISAR) measured the time-resolved velocity at the interface between the ceramic and the lithium-fluoride window [Barker and Hollenbach, 1972; Wise and Chhabildas, 1986]. The measured velocity profiles are shown in Figure 12. Impact of

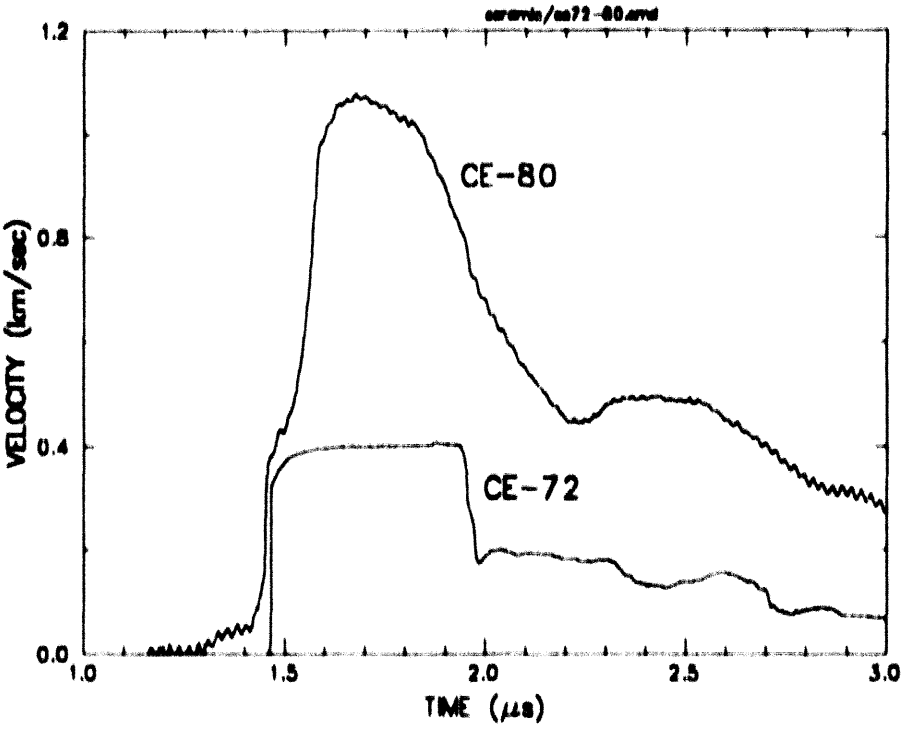

Figure 12. Interface velocity profiles for aluminum oxide impact experiments.

the thin ceramic sample mounted in the projectile, which is in turn backed by polyurethane foam, led to the propagation of a compressive shock and release wave in the target ceramic. Details of this wave are recorded in the measured VISAR velocity profile. The interaction of release waves within the target ceramic sample also leads to a test of the dynamic tensile (spall) strength of the ceramic. Pertinent experimental parameters are provided in Table 5.

Table 5:
Experimental Parameters for Aluminum Oxide Impact Test

Test Number	Foam Density (kg/m^3)	Target Thickness (mm)	Impactor Thickness mm	Impact Velocity (km/s)
CE-72	145	6.230	2.804	0.587
CE-80	640	6.261	2.802	1.855

Analysis

Compressive stress state data (Hugoniot states) determined by wave analysis of the measured VISAR profiles are provided in Table 6.

Table 6:
Hugoniot Data for Aluminum Oxide Impact Test

Test Number		Shock Velocity (km/s)	Particle Velocity (km/s)	Stress (GPa)	Specific Volume (m^3/kg)	Pullback Velocity (m/s)	Spall Stress (GPa)
CE-80	Elastic State	11.24	0.267	11.9	0.2459		
	Final State	9.35	0.927	36.4	0.2281	43	1.2
CE-72	Elastic State	11.24	0.220	9.8	0.2470		
	Final State	10.75[a]	0.293	12.9	0.2452	<20	< 0.5

[a] Shock velocity determined from time at midpoint amplitude between elastic break and peak particle velocity.

The velocity of the elastic wave reported in Table 6 is based on the longitudinal ultrasonic velocity of 10.9 km/s and a finite strain nonlinearity at the Hugoniot elastic limit determined from a linear shock-velocity versus particle-velocity slope of $S = 1.25$.

The lower amplitude profile (CE-72) in Figure 12 indicates onset of dynamic yield at about 10 GPa. This compares with an HEL of about 11.9 GPa calculated for Test CE-80. Such variations are typical for materials in which the dynamic yield is sensitive to the strain rate in, and degree of evolution of, the following deformation wave (see the background in Section 2 of this report). For comparison, the Hugoniot elastic limit measured on other aluminum oxide ceramics with VISAR methods is somewhat lower. The Hugoniot elastic limit for Coors AD-995 measured at Sandia is approximately 6.2 GPa. Munson and Lawrence (1979) measured an HEL of 9.1 GPa on General Electric Lucalox. Recent measurements on Coors AD-999, however, are comparable with the present data.

The final Hugoniot state for test CE-80 is based on a symmetric impact, and the measured projectile velocity and second-wave shock velocity. The peak amplitude of the particle velocity profile is not consistent with the calculated Hugoniot state, being about 5% to 10% low. The wave is not flat topped and some attenuation due to the overtaking release wave may have occurred. The gradual precompression prior to arrival of the elastic shock at about 1.6 μs for the CE-80 profile is probably a consequence of a small particle trapped between the impacting plates during the test. Reverberation of the wavelet caused by this experimental complication may have also effected the peak amplitude of the profile.

Also of interest is the dynamic tensile strength of this aluminum oxide as inferred from the spall pullback signal observed in the wave profile. Based on an acoustic approximation, the spall stress is,

$$\frac{1}{2}(Z_1 + Z_2)\,\Delta u_{pb}\,, \tag{6}$$

where Z_1 and Z_2 are the mechanical impedance of aluminum oxide and lithium fluoride, respectively, and Δu_{pb} is the measured pullback velocity. The pullback signal for Test CE-80 is illustrated in Figure 13 and provides a spall strength of about 1.2 GPa. Although the

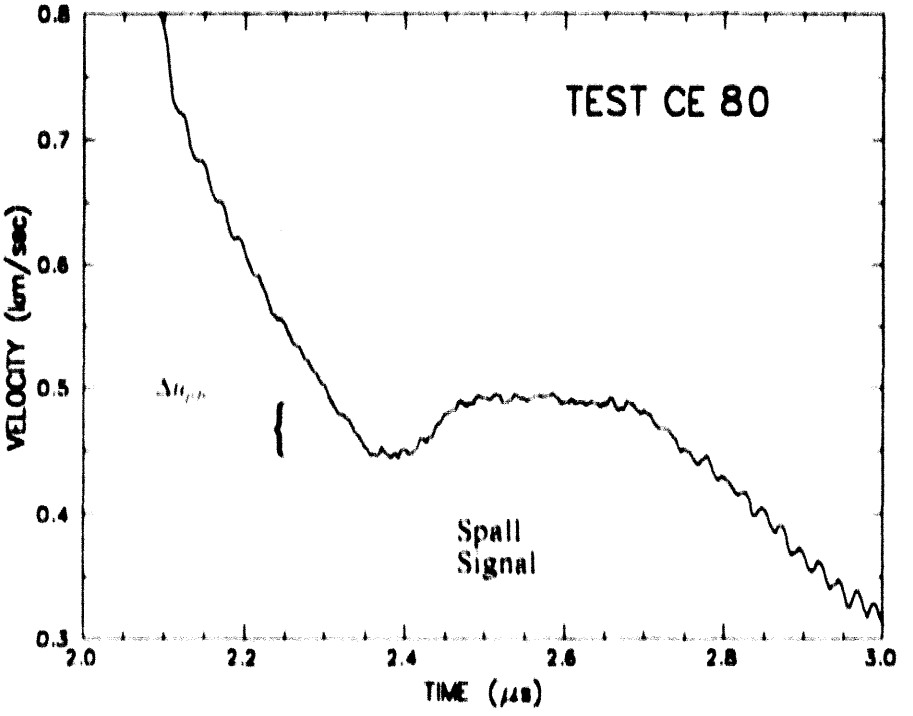

Figure 13. Velocity-profile spall pullback signal

results from one test are always open to question, a dynamic tensile strength of this magnitude is unusually high for ceramics. Typical spall strengths for ceramics are about 0.2-0.5 GPa. Higher values have been observed only for a very high-density, fined-grained zirconia (Grady and Mashimo, 1992) for which a spall strength of 1.6 GPa was determined. More important is the shock precompression of this sample to approximately 36 GPa before the tensile spall strength is tested.

In contrast, Test CE-72 which just exceeds the HEL of this material, indicates a spall strength of 0.5 GPa or less. (There is some uncertainty in the wave structure in this region.) Similar measurements on Lucalox by Munson and Lawrence (1979) also revealed negligible spall strength in experiments exceeding the Hugoniot elastic limit on precom-

pression. They attributed the loss of tensile strength to pervasive microcracking during shock compression. It appears reasonable to suggest that the fine-grained homogeneous microstructure of the present alumina leads to enhanced plasticity under the more intense deformation of the higher-amplitude shock compression experiment. Lack of significant microcracking could lead to the substantial dynamic tensile strength observed in this experiment. These results would tend to support the model of Cagnoux and Longy (1988) for the shock deformation behavior of alumina with and without glassy phases in which issues of homogeneous and heterogeneous microstructures are also addressed. Less intense deformation experienced in the lower amplitude test may encourage microcracking and hence reduced spall strength.

Shock Recovery Experiments

Several shock recovery experiment on the same high-quality aluminum oxide ceramic were also performed. The geometry of the projectile and the recovery target fixture are sketched in Figure 14. The experiment was performed on a small two-stage light gas gun with a 12 mm launch tube diameter. An aluminum plate mounted on a lexan sabot constituted the projectile. The aluminum oxide sample was contained in a steel (4340, Rc 40) holder as shown. The aluminum oxide was backed by copper (a momentum trap to minimize strong tensile states during pressure release) which in turn was backed by ten-pound-per-cubic-foot polyurethane foam. The contents were held in place with a 1/2 in. - #13 threaded bolt.

Two sample assemblies were shock loaded and recovered. Impact velocities were about 1.5 and 2.0 km/s. Shock stress levels of 17.5 and 25.0 GPa, respectively, have been calculated through impedance matching methods. Preliminary analysis of the shock-recovered aluminum oxide have been performed by Staehler and Predebon, Michigan Technological University.

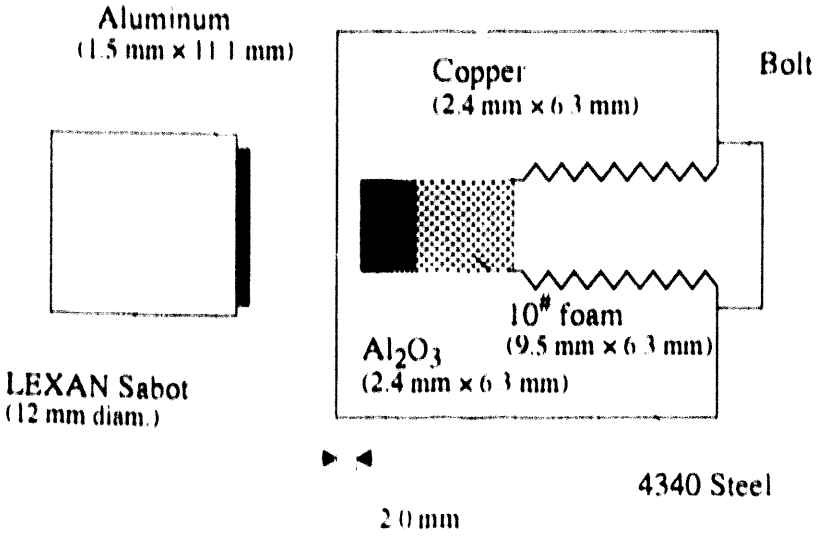

Figure 14. Shock recovery assembly.

7. Failure Properties of High-Density Glass

A series of plate-impact experiments was completed at SNL as part of the collaborative effort initiated by R. J. Clifton and G. F. Raiser, Brown University (BU), and SNL personnel to examine dynamic failure mechanisms in glass. These experiments, performed on a single-stage propellant (powder) gun, utilized a velocity interferometer, or VISAR [Barker and Hollenbach, 1972], to obtain time-resolved loading and unloading data which permitted determination of Hugoniot and spall parameters for specially prepared samples of an aluminosilicate glass (Corning No. 1723). In addition, the measured velocity histories complemented separate studies at BU of the post-shock morphology of ceramic samples (Al_2O_3) by providing an independent, dynamic database for a material with composition similar to the intergranular glassy phase present in the ceramic. Information from this database was appropriate for assessing the existence and properties of a "failure wave," similar to that noted by other investigators [Bless, *et al.*, 1990; Bless, *et al.*, 1992], which has been reported to originate at the impact surface of pyrex and soda-lime glass samples and subsequently trail behind the initial transmitted shock. The interferometer records from the SNL test series were analyzed to obtain particle-velocity histories, Hugoniot data, and spall-strength estimates for the aluminosilicate glass. In addition, features of the velocity histories were examined with regard to evidence of failure-wave propagation.

Experimental Configuration

The tests considered in this report (designated GLASS1, 2, 3, and 4) involved target assemblies incorporating specimens of aluminosilicate glass in a nominally one-dimensional (uniaxial strain) impact geometry. The test configuration is illustrated in Figure 15. For

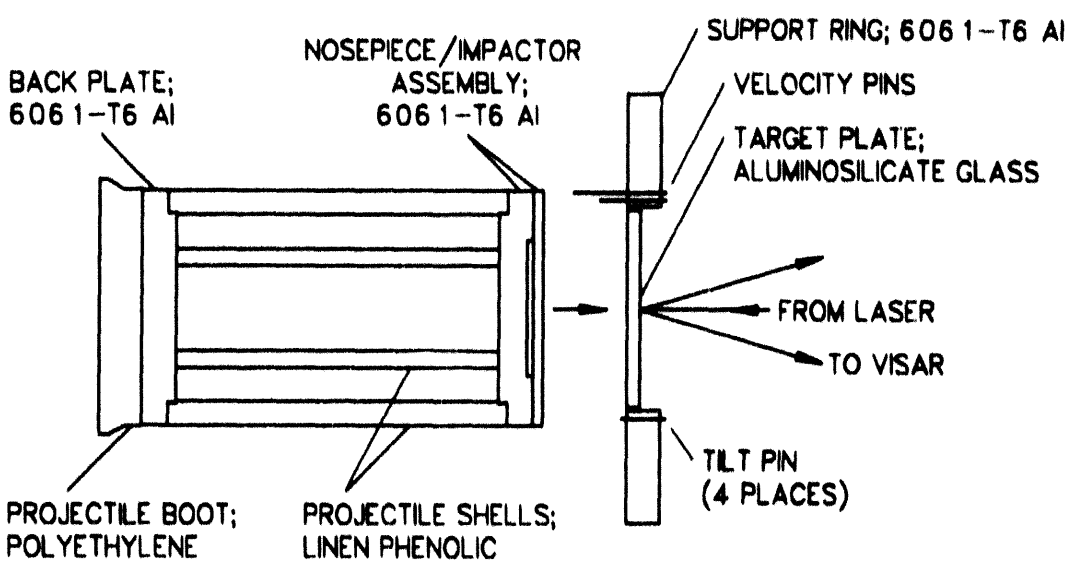

Figure 15. Experimental configuration for shock/release/spall and failure-wave investigations on aluminosilicate glass (tests GLASS1-4).

each test, an aluminum impactor plate was used to provide initial loading of the glass through a right-going shock, followed by unloading through a right-going rarefaction originating at the impactor rear (free) surface. Interaction within the glass of this right-going rarefaction with the initial left-going rarefaction originating at the glass free surface produced tensile stress states suitable for evaluation of the spall strength of the glass. The tests were conducted at two different impact stresses, ~ 8 GPa (tests 1 and 2) and ~ 3 GPa (tests 3 and 4), and involved nominally 5-mm thick glass targets prepared at BU with impact surfaces that were either polished (tests 1 and 3, 0.01-0.07 μm RMS roughness) or deliberately abraded (tests 2 and 4, 0.51-0.53 μm RMS roughness). These different surface treatments were used to determine the influence, if any, of initial defect density and amplitude on the structure of the resultant wave profile--particularly the effect on failure-wave initiation and evolution. In all cases, the rear (free) surface of the glass was highly polished and coated with a thin film of aluminum to provide a specularly reflective surface for laser light.

Dynamic loading of a glass target plate was produced by a flat-faced projectile that was accelerated to a preselected impact velocity (0.96 km/s for shots 1 and 2; 0.45 km/s for shots 3 and 4) by the powder gun. The forward element of the projectile assembly consisted of a 6061-T6 aluminum impactor plate which was nominally 3.6-mm thick. The impactor was bonded to a projectile nosepiece which had a counterbore in its front face that left the central portion of the impactor unsupported, thereby providing maximum stress release through the initial right-going rarefaction transmitted into the glass target. Coaxial shorting pins mounted around the support-ring periphery allowed measurements of impact velocity and tilt.

For all experiments, the particle-velocity history at the glass free surface was measured using a velocity interferometer system, VISAR [Barker and Hollenbach, 1972], with an argon-ion laser light source (wavelength = 514.5 nm). The free-surface velocity histories obtained for shots GLASS1, 2, 3, and 4 are shown in Figure 16, where time $t = 0.00$ μs corresponds to first contact of the impactor with the glass target. For all experiments, the VISAR records initially indicated a finite-risetime compressional loading to a steady free-surface velocity. The arrival time of the leading break, or "toe," of this wavefront corresponded, within experimental uncertainty, to that expected for an impact-generated disturbance propagating through the glass at the longitudinal sound speed. The initial free-surface *loading* histories from all four tests are plotted together for comparison in Figure 17 which demonstrates that dispersive loading waveforms were obtained in all cases, with a characteristic risetime to the peak stress state of about 50 ns for the two low-pressure tests (3 and 4) and about 220 ns for the two high-pressure tests (1 and 2).

Hugoniot States

As discussed above, the leading compressional wavefronts transmitted through the glass did not show any sharp shocks, and it was not evident that the elastic limit of this material had been exceeded in any of these experiments. Consequently, an impedance-matching determination of Hugoniot parameters on the basis of the shock velocity in the glass was inappropriate. Instead, the *in situ* particle velocity behind the leading compression (estimated to be one-half the peak free-suface equilibrium velocity) was taken as the Hugoniot

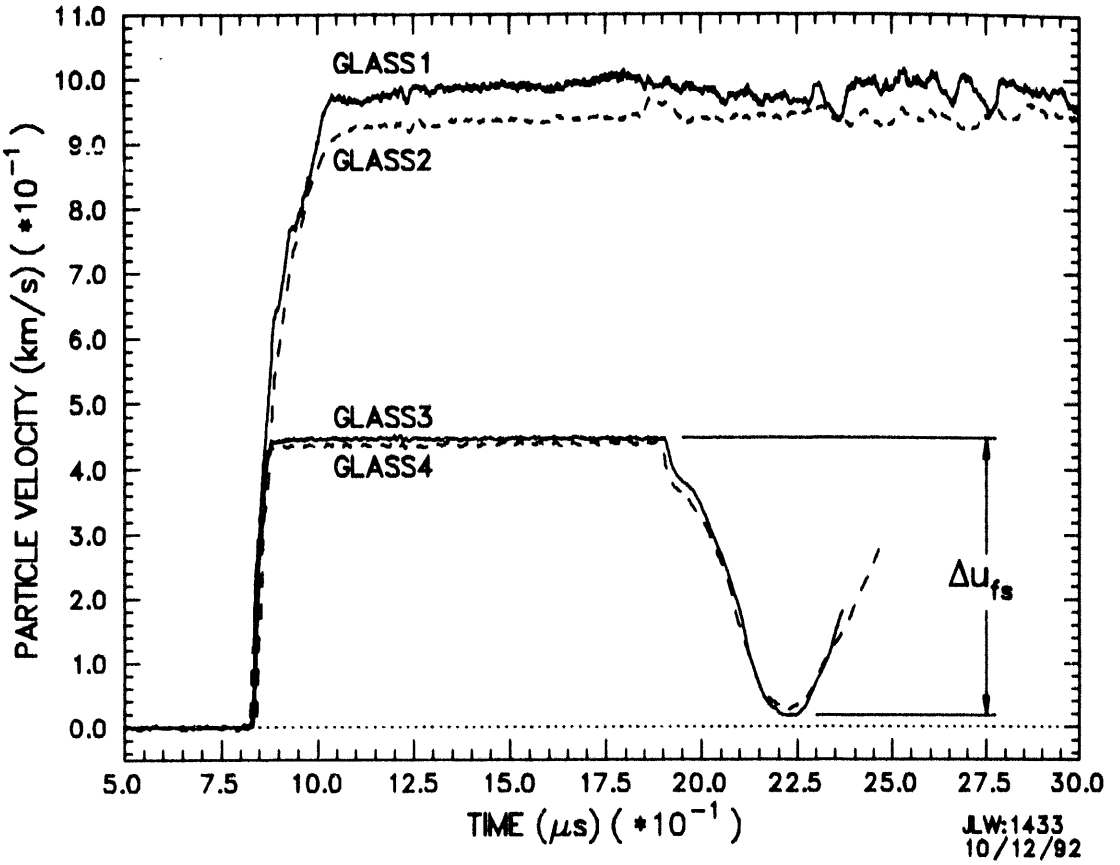

Figure 16. Free-surface velocity histories for shots GLASS1-4.

particle velocity (u_{PH}) and used with the reported Hugoniot data for 6061-T6 aluminum [Marsh, 1980] to determine the impact stress, which was equivalent to the Hugoniot pressure (P_H) in the glass. The experimental Hugoniot particle-velocity and pressure parameters for the glass specimens tested in shots 1 through 4 are summarized below in Table 7:

Table 7:
Hugoniot Parameters for Aluminosilicate Glass

Shot Number	u_{PH} (km/s)	P_H (GPa)
1	0.485	7.70
2	0.464	8.15
3	0.223	3.47
4	0.218	3.44

Spall Observations

For these tests, the impactor was sufficiently thin to allow full transmission of the initial right-going rarefaction originating at its rear surface into the glass target where it interacted with the initial left-going rarefaction originating at the glass free surface. For the low-stress tests (3 and 4), as seen in Figure 16, arrival at the glass free surface of the initial rarefaction from the impactor rear surface is manifested by a period of decreasing velocity which begins at $t \approx 1.90$ μs after impact, and ends with attainment of a local minimum velocity at $t \approx 2.23$ μs. The observed change in free-surface velocity, Δu_{fs}, between the peak loading state and this local minimum may be related to the level of tensile stress, σ_T, supported by the glass using the relation $\sigma_T \approx \frac{1}{2}\rho_0 C_l (\Delta u_{fs})$, where ρ_0 and C_l are, respectively, the initial glass density and longitudinal sound speed. For tests 3 and 4, Δu_{fs} had values of 0.429 and 0.412 km/s, respectively, corresponding to calculated values for σ_T of 3.49 and 3.35 GPa. In cases where the glass fractures, σ_T is equal to the spall strength of the material. For the current tests, the shock impedance of the aluminum impactor closely matched that of the glass, so essentially full release of the glass was possible if no spall occurred. Since the observed velocity histories for tests 3 and 4 showed approximately full release (*i.e.*, $\sigma_T \approx P_H$), the reported values represent *lower bounds* on the spall strength of the glass following shock compression to 3.4-3.5 GPa.

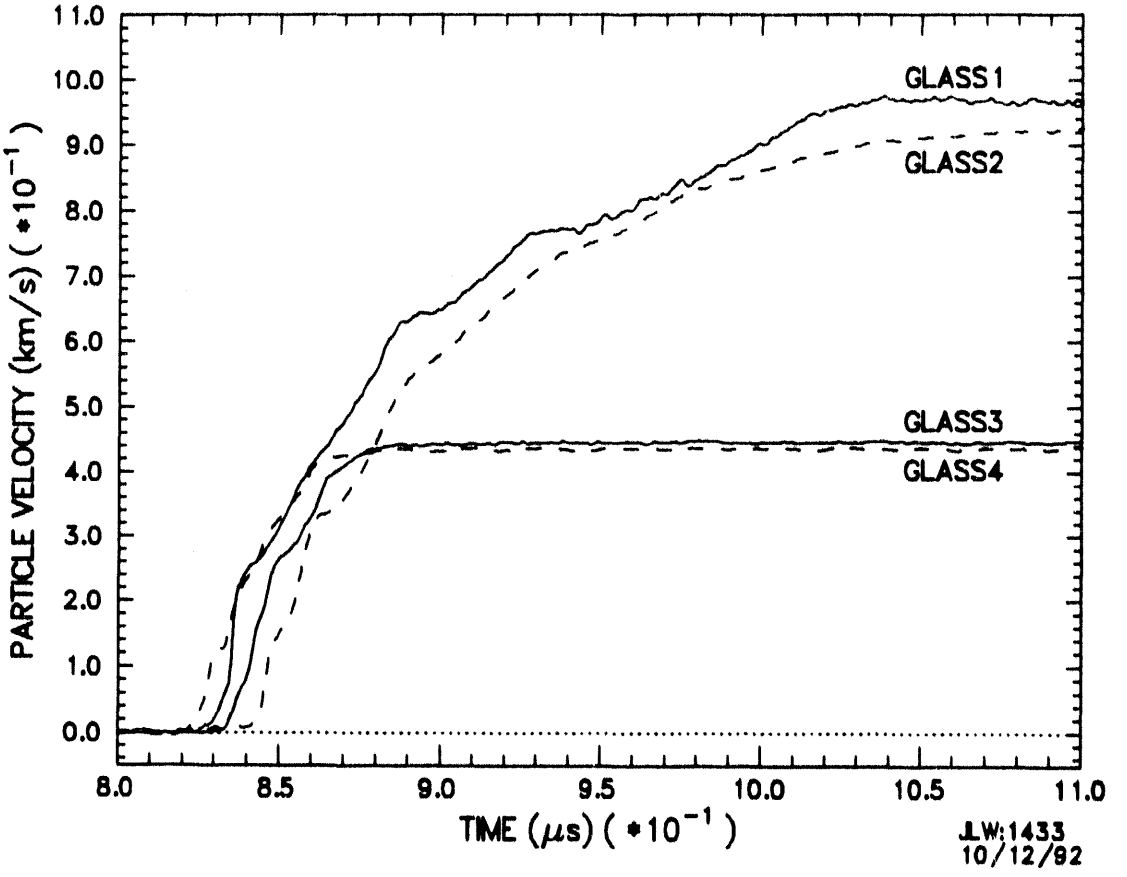

Figure 17. Expanded view of loading histories for shots GLASS1-4.

For experiments 1 and 2, a period of decreasing velocity beginning at $t \approx 1.90$ μs after impact was not discernible in the VISAR records, and the free-surface velocity remained essentially at its peak value for the duration of the recording time. On this basis, it was concluded that the glass samples *did* spall during tests 1 and 2, and that the spall strength of aluminosilicate glass was negligible after shock compression to 7.7-8.2 GPa.

Failure Wave Analysis

Assuming that a failure wave was generated at impact and propagated into the glass target at a velocity given by $C_R/(\ 2) = 2.29$ km/s [Raiser, 1992], where C_R = Rayleigh-wave speed, then the leading characteristics of the release wave from the glass free surface should have interacted with the failure front and returned to the free surface at a time $t \approx 1.55$ μs relative to impact. Examination of the velocity histories for all four experiments showed no conclusive evidence for the arrival of a disturbance at this time. This result indicated that either (1) no failure front had been generated, or (2) the impact-direction impedance mismatch across the failure front was quite small. The wave-profile data also imply that failure-wave formation may not necessarily be a consequence of impact-surface defects.

8. Conclusions/Future Work

The present document reports progress on a range of activities focused on the dynamic mechanical properties of ceramic materials. Impact equation-of-state experiments on monolithic ceramics including titanium diboride and aluminum oxide have revealed important influences of microstructure on the dynamic strength and rheological properties of these materials. An extensive correlation of indentation hardness and impact strength properties of ceramics has been performed which contributes to the understanding of ceramic yield and failure. A methodology for measuring the hydrodynamic response of ceramics through shock-wave experiments on metal-ceramic composites has been developed. Dynamic pressure-volume data for silicon carbide has been obtained. A technique for determining dynamic multiaxial properties of ceramics has been developed through impact experiments on confined and unconfined ceramic rods using longitudinal and transverse VISAR diagnostics. Experiments on high-density glass have been performed to address issues of dynamic fracture and failure wave propagation.

A range of further activities has been stimulated by the progress of the present material properties research. These activities will be pursued within the present program over the next year.

Further shock equation-of-state and dynamic strength experiments on selected monolithic armor ceramics will continue. These tests will focus on specific needs of the computational modelling community and will include ceramics with improved microstructure, and shock data at higher impact velocities. A suite of impact tests on Coors AD-999 alumina ceramic is currently being pursued to address porous material issues in modeling the Coors AD-995 previously tested. Also of concern is the high-purity fine-grain titanium diboride ceramic currently being considered for ballistic applications. Higher velocity impact experiments on silicon carbide and boron carbide will be performed to complement earlier data and address specific modeling needs.

Measurement of the hydrodynamic properties of ceramics through shock testing on metal-ceramic composites, which has been successfully developed over the past year, is yielding unexpected results on silicon carbide and titanium diboride. These studies are impacting computational model development, and the research will continue within the next year to address the material modeling implications.

The testing of multiaxial properties of armor ceramics through impact experiments on confined and unconfined ceramic rods with axial and transverse VISAR diagnostics represented a substantial development within the past year and very encouraging results have emerged from this work. The effort will continue next year with emphasis focused on supporting computational analysis and optimization of geometry to increase sensitivity to multiaxial strength properties of the test ceramics.

9. References

Adadurov, G. A., A. N. Dremin, S. V. Pershin, *et al.*, *Zh. Prikl. Mech. Tekh. Fiz.* 4, 81, 1962.

Ahrens, T. J., W. H. Gust and E. B. Royce, *J. Appl. Phys.*, 39, 4610, 1968.

Barker, L. M., and R. E. Hollenbach, *J. Appl. Phys.* 43, 4669, 1972.

Bless, S. J., N. S. Brar, and Z. Rosenberg, in: Shock Compression of Condensed Matter - 1989, edited by S. C. Schmidt, J. N. Johnson, and L. W. Davison (Elsevier Science Publishers B. V., New York), 939, 1990.

Bless, S. J. , N. S. Brar, G. Kanel, and Z. Rosenberg, *J. Am. Ceram. Soc.* 75, 1002, 1992.

Cagnoux, J. and F. Longy, DYMAT 88 - International Conference on Mechanical and Physical Behaviour of Materials under Dynamic Loading. les editions de physique, C3-3, 1988.

Cline, C. F., March, 1989. (private communication)

Dandekar, D. P., and D. C. Benfanti, *J. Appl. Phys.* (to be published), 1992.

Gilman, J. J., *J. Appl. Phys.* 41, 1664, 1970.

Grady, D. E., and M. D. Furnish, Sandia National Laboratories Technical Report SAND88-1642, December 1988.

Grady, D. E., in: Shock Compression of Condensed Matter-1991, edited by S. C. Schmidt, R. D. Dick, J. C. Forbes, and D. G. Tasker (Elsevier Science Publishers B. V. New York), 455, 1992.

Grady, D. E., Proceedings of the XIII International AIRAPT Conference, Bangalore, India, October 7-11, 1991.

Grady, D. E., and T. Mashimo, *J. Appl. Phys.* 71, 4868, 1992.

Graham, R. A., and W. P. Brooks, *Phys. Chem. Solids*, 32, 2311, 1971.

Gust, W. H., and E. B. Royce, *J. Appl. Phys.* 42, 276, 1971.

Gust, W. H., A. C. Holt, and E. B. Royce, *J. Appl. Phys.* 42, 276, 1973.

Holmquist, T. J., Alliant Techsystem Report, October 1991.

Kanel', G. I., and A. N. Pityulin, *Fizika Goreniya i Vzryva* 28, 85, 1984.

Kipp, M. E., and D. E. Grady, Sandia National Laboratories Technical Report SAND89-1461, July 1989a.

Kipp, M. E., and D. E. Grady, in: Shock Compression of Condensed Matter-1989, edited by S. C. Schmidt, J. N. Johnson, and L. W. Davison (Elsevier Science Publishers B. V New York), 377, 1990.

Kipp, M. E., and R. J. Lawrence, Sandia National Laboratories Technical Report SAND81-0930, June 1982.

Kovtun, V. I., and I. I. Timofeeva, *Poroshkovaya Metallurgiya* 8, 92, 1988.

Marsh, S. P.,editor, LASL Shock Hugoniot Data., University of California Press, 1980.

Mashimo, T., Y. Hanaoko, and K. Nagayama, *J. Appl. Phys.* 63, 327, 1988.

McQueen, R. C., and S. P. Marsh, Handbook of Physical Constants, edited by S. P. Clark Jr., Geophysical Society of America, New York, Chapter 7, 1960.

Munson, D. E., and R. J. Lawrence, Dynamic Deformation of Polycrystalline Alumina, *J. Appl. Phys.*, 50, 6272, 1979.

Poduretz, M. A., G. V. Simkov, and R. F. Trunin, *Izvestiya, Earth Physics* 24, 267, 1988.

Raiser, G. F., Brown University, July 1992 (private communication).

Rosenberg, Z., N. S. Brar, and S. J. Bless, *J. Appl. Phys.* 70, 167, 1991.

Slavin, M. J., ARL, August 1991 (private communication).

Staehler, J. M., W. W. Predebon, and B. J. Pletka, Proceedings, Army Symposium on Solid Mechanics, Plymouth, Massachusetts, November, 1991.

Swegle, J. W., Sandia National Laboratories Technical Report SAND81-2235, December 1981.

Swegle, J. W., Sandia National Laboratories, March 1992 (private communication).

Tang, Z. P., and Y. M. Gupta, *J. Appl. Phys.* 64, 1827, 1988.

Taylor, G., *Proc. Roy. Soc. London Series A* 194, 289, 1948.

Winkler, W. D., and A. J. Stilp, in: Shock Compression of Condensed Matter-1991, edited by S. C. Schmidt, R. D. Dick, J. C. Forbes, and D. G. Tasker (Elsevier Science Publishers B. V. New York), 555, 1992.

Winkler, W. D., Ernst-Mach Institute, October 21, 1991 (Technical Exchange).

Wise, J. L., and L. C. Chhabildas, in: Shock Waves in Condensed Matter, edited by Y. M. Gupta, (Plenum, New York), 441, 1986.

Yeshurin, Y., D. G. Brandon, A. Venkert and Z. Rosenberg, DYMAT 88 - International Conference on Mechanical and Physical Behaviour of Materials under Dynamic Loading. les editions de physique, C3-11, 1988.

DISTRIBUTION:

INTERNAL

1400 E. H. Barsis
1402 S. J. Dosanjh
1403 G. S. Davison
1404 J. A. Ang
1421 W. J. Camp
1422 R. C. Allen
1423 E. F. Brickell
1424 A. L. Hale
1425 J. H. Biffle
1431 J. M. McGlaun
1431 K. G. Budge
1431 E. S. Hertel
1431 R. J. Lawrence
1431 J. S. Peery
1431 A. C. Robinson
1431 T. G. Trucano
1431 M. K. Wong
1432 P. Yarrington
1432 P. J. Chen
1432 H. E. Fang
1432 A. V. Farnsworth
1432 G. I. Kerley
1432 M. E. Kipp
1432 S. A. Silling
1432 P. A. Taylor
1433 P. L. Stanton
1433 J. A. Ang
1433 L. C. Chhabildas
1433 M. D. Furnish
1433 D. A. Crawford
1433 D. E. Grady (25)
1434 D. R. Martinez
1500 D. J. McCloskey
1511 J. S. Rottler
1512 A. C. Ratzel
1561 H. S. Morgan
1562 R. K. Thomas
1562 J. W. Swegle
2565 S. T. Montgomery
6100 R. W. Lynch
6111 J. C. Dunn
6111 J. L. Wise (15)
7141 Technical Library (5)
7151 Technical Publications
7613 Document Processing for DOE/OSTI (10)
8523-2 Central Technical Files
9702 W. Tucker
9723 M. J. Forrestal
9723 V. K Luk

EXTERNAL

T. F. Adams
Los Alamos National Laboratory
MS F663
Los Alamos, NM 87545

T. J. Ahrens
Geophysics Division MS/252-21
California Institute of Technology
Pasadena, CA 91125

F. Allahdadi
Phillips Laboratory
PL/WSSD
Kirtland AFB, NM 87117-6008

M. L. Alme
102 Stevens Forrest Professional Center
9650 Santiago Road
Columbia, MD 21045

C. E. Anderson
Southwest Research Institute
6220 Culebra Road
San Antonio, TX 78284

D. W. Baum
Lawrence Livermore National Laboratory
Livermore,CA 94550

S. J. Bless
Institute for Advanced Technology
4030-2 W. Braker Lane
Austin, TX 78759-5329

W. Blumenthal
Los Alamos National Laboratory
MS E546
Los Alamos, NM 87545

W. J. Bruchey
U.S. Army Research Laboratory
SLCBR-TB-A
Aberdeen Proving Ground, MD 21005-5066

S. Chou
Army Research Laboratory
Materials Directorate
AMSRL-MA-DA
Watertown, MA 02172-0001

R. Clifton
Brown University
Division of Engineering
Providence, RI 02912

J. A. Collins
U.S. Air Force Armament Laboratory
AD/MNW
Eglin Air Force Base, FL 32542-5434

J. W. Coltman
Simula Inc.
10016 South 51st Street
Phoenix, AZ 85044

E. Cort
Los Alamos National Laboratory
MS K574
Los Alamos, NM 87545

J. W. Coltman
Simula Inc.
10016 South 51st Street
Phoenix, AZ 85044

D. Curran
SRI International
333 Ravenswood Avenue
Menlo Park, CA 94025

D. Dandekar
U.S. Army Research Laboratory
Materials Directorate
AMSRL-MA-DA
Watertown, MA 02172-0001

K. Epstein
DOW Chemical USA
Ordnance Systems, 800 Building
Midland, MI 48667

P. Follansbee
Los Alamos National Laboratory
MS K663
Los Alamos, NM 87545

J. C. Foster, Jr.
U.S. Air Force Armament Laboratory
AD/MNW
Eglin Air Force Base, FL 32542-5434

Y. Gupta
Washington State University
Department of Physics
Pullman, WA 99163

G. Hauver
U.S. Army Research Laboratory
AMSRL-WT-TA
Aberdeen Proving Ground, MD 21005-5066

T. Holmquist
Alliant Techsystems, Inc.
7225 Northland Drive
Brooklyn Park, MN 55428

Y. Horie
North Carolina State University
Dept. of Civil Engineering
Raleigh, NC 27607

K. Iyer
U.S. Army Research Office
P. O. Box 12211
Research Triangle Park, NC 27709

G. Johnson
Alliant Techsystems, Inc.
7225 Northland Drive
Brooklyn Park, MN 55428

J. N. Johnson
Los Alamos National Laboratory
MS B221
Los Alamos, NM 87545

K. Kimsey
U.S. Army Research Laboratory
Attn: SLCBR-TB-P
Aberdeen Proving Ground, MD 21005-5066

R. W. Kocher
Defense Advanced Research Projects Agency
Land Systems Office
3701 North Fairfax Drive
Arlington, VA 22203-1714

J. Lankford
Southwest Research Institute
6220 Culebra Road
San Antonio, TX 78284

K. T. Leighton
Lanxide Armor Products, Inc.
1300 Marrows Road
P. O. Box 6077
Newark, DE 19714-6077

D. Mandell
Los Alamos National Laboratory
MS F663
Los Alamos, NM 87545

M. Manghnani
Mineral Physics Group
University of Hawaii
2525 Correa Rd.
Honolulu, HA 96822

P. Maudlin
Los Alamos National Laboratory
MS K557
Los Alamos, NM 87545

H. C. Meyer
U.S. Army Research Laboratory
AMSRL-WT-TA
Aberdeen Proving Ground, MD 21005-5066

M. Meyer
Univ. of Calif. at San Diego
Dept. of Applied Mech. & Eng. Sciences
La Jolla, CA 92093

J. D. Morrow
FMC Corporation
Ground Systems Division
1107 Coleman Avenue Box 367
San Jose, CA 95103

S. Nemat-Nasser
Univ. of Calif. at San Diego
Dept. of Applied Mech. & Eng. Sciences
La Jolla, CA 92093

T. Nicholas
Air Force Wright Aeronautical Labs.
Air Force Systems Command
Materials Laboratory
Wright-Patterson AFB, OH 45433

D. Orphal
California Research and Technology, Inc.
5117 Johnson Drive
Pleasanton, CA 94566

R. Palicka
CERCOM, Inc.
1960 Watson Way
P. O. Box 70
Vista, CA 92083

R. Paricio
Coors Ceramics Company
600 Ninth Street
Golden, CO 80401

W. W. Predebon
College of Engineering
Michigan Technological University
Houghton, MI 49931

G. F. Raiser
Washington State University
Department of Physics
Pullman, WA 99163

A. M. Rajendran
Army Research Laboratory
Materials Directorate
AMSRL-MA-DA
Watertown, MA 02172-0001

G. Randers-Pehrson
U.S. Army Ballistic Research Laboratory
SLCBR-TB-W
Aberdeen Proving Ground, MD 21005-5066

M. Scheidler
U.S. Army Research Laboratory
AMSRL-WT-TD
Aberdeen Proving Ground, MD 21005-5066

P. Schneiwind
California Research and Technology, Inc.
5117 Johnson Drive
Pleasanton, CA 94566

S. Segletes
U.S. Army Research Laboratory
SLCBR-TB-W
Aberdeen Proving Ground, MD 21005-5066

D. A. Shockey
Poulter Laboratory
SRI International
333 Ravenswood Avenue
Menlo Park, CA 94025

R. Skaggs
Los Alamos National Laboratory
MS K574
Los Alamos, NM 87545

M. Slavin
U.S. Army Research Laboratory
SLCMT-MCC
Arsenal Street
Watertown, MA 02172-0001

J. M. Staehler
College of Engineering
Michigan Technological University
Houghton, MI 49931

D. Steinberg, MS L35
Lawrence Livermore National Laboratory
P. O. Box 808
Livermore, CA 94550

J. Sternberg
Naval Postgraduate School
Superintendent Code 412B
Monterey, CA 93943

D. J. Viechniki
U.S. Army Research Laboratory
SLCMT-MCC
Arsenal Street
Watertown, MA 02172-0001

T. Wright
U.S. Army Research Laboratory
SLCBR-TB-W
Aberdeen Proving Ground, MD 21005-5066

DATE FILMED

11/22/93

END